PHILOSOPHICAL TRANSACTIONS OF THE ROYAL SOCIETY A MATHEMATICAL, PHYSICAL & ENGINEERING SCIENCES

Acoustic Microscopy from 10 to 100 MHz for Industrial Applications [and Discussion]

R. S. Gilmore, K. C. Tam, J. D. Young, D. R. Howard and E. Almond

Phil. Trans. R. Soc. Lond. A 1986 **320**, 215-235
doi: 10.1098/rsta.1986.0112

Phil. Trans. R. Soc. Lond. A **320**, 215–235 (1986)
Printed in Great Britain

Acoustic microscopy from 10 to 100 MHz for industrial applications

By R. S. Gilmore[1], K. C. Tam[1], J. D. Young[1] and D. R. Howard[2]

[1] *General Electric Company, Corporate Research and Development, Schenectady, New York* 12345, *U.S.A.*

[2] *Tartan Minicomputer Applications Company, Rensselaer, New York* 12144, *U.S.A.*

[Plates 1–4]

The development of a system is described here that, for the first time, utilizes acoustic microscopy techniques to evaluate materials and processes on a scale practical for support of automated manufacture. The properties of acoustic microscopy attractive for this application are the ability to inspect the elastic structure of the surface and the subsurface of materials. In the past, several barriers have prevented its use except for near-surface inspection of a very limited area (a few square millimetres). These barriers include critical alignment requirements, very shallow penetration, and limitations in resolution and the size of the workpiece.

Presented here is a unique configuration that differs from high-frequency or conventional acoustic microscopy methods in these ways:

(*a*) images are formed directly by displaying amplitude of *broadband* acoustic pulses (centre frequencies: 10–100 MHz; bandwidths: 80%–120%), rather than by displaying amplitude variations resulting from interference between *narrowband* pulses (carrier frequencies: 0.5–4.0 GHz; bandwidths: 0.5%–1.0%);

(*b*) the short pulses, having only a 2–4 wavelength duration, are readily time resolved by gating the surface wave and thus eliminating interference from the direct reflection. This technique avoids the complex analytical problem of separating the surface waves from the direct reflection;

(*c*) a single-crystal silicon acoustic lens is used instead of the sapphire acoustic lens conventionally used.

Incorporating these methods, a large-scale, 10–100 MHz scanning microscopy system has been developed with the following advances over previously reported ultrasonic non-destructive testing systems and acoustic microscopes:

(*a*) reliable detection and display of surface-breaking cracks is possible at all orientations for non-destructive evaluation purposes;

(*b*) imaging accuracy is *independent of* small variations in the water gap (the distance between lens and workpiece); in contrast, such variations are a major consideration in determining the imaging quality of conventional acoustic microscopes;

(*c*) magnifications of 2–20 times instead of 1000 times allow interrogation of much larger areas and volumes of material;

(*d*) the compound resolution of large against small features is theoretically explained for the first time by a combined ray tracing–diffraction model;

(*e*) a practical method for the inspection of volumes and even interior surfaces results from the use of longer wavelength signals, where previously the use of shorter wavelength signals limited penetration to the first few micrometres of the subsurface;

(*f*) shear-wave images of subsurface features, which give the most dependable information on the integrity of bonded interfaces, are available, as well as longitudinal-wave images.

Practical applications are presented, such as inspection for near-surface inclusions in

aircraft engine materials and inspection of heat-sink bonds in semiconductor power devices.

The broadband-wave method presented here allows scanning acoustic-microscopy methods, previously available only on a scale useful for the materials scientist, to be used on a scale practical for industrial materials evaluation, with a capability for an interrogated volume 12 orders of magnitude greater than that possible with the higher frequency methods.

1. Introduction

Since its introduction more than a decade ago, scanning acoustic microscopy, after Lemons & Quate (1973, 1974) and Quate *et al.* (1979), has provided a new creditability and dimension to acoustic imaging. Nearly three decades after Sokoloff (1950) suggested the concept, the technology had finally advanced to a state in which c-scan acoustic images could be produced with equivalent resolution and detail to those produced with the highest-quality optical microscopes. Subsequent work by Saad *et al.* (1974), Weglein (1978, 1985), Parmon & Bertoni (1979), Bertoni (1984), Bertoni & Tamir (1973), Wickramasinghe (1978), Bennett & Ash (1980), Sheppard & Wilson (1981), Smith *et al.* (1983), Nikoonahad *et al.* (1985), Kino (1980), Liang *et al.* (1985*a*, *b*), and many other investigators has improved our knowledge of both surface and subsurface acoustic microscopy so that today it is one of the more versatile materials characterization methods that is available to the scientist or engineer.

All the published work to date clearly indicates that industrial acceptance tests can be developed at much lower frequencies (and much greater fractional bandwidths) by using similar concepts and greatly scaled up hardware. The need for this is also clearly apparent. There is a gap of at least 12 orders of magnitude in the inspection volume between the study and characterization of tens of thousands of cubic micrometres of material, with 1 GHz acoustic microscope forming images at a magnification of 1000 and the evaluation of the order 10^4 cm^3 of material, for use in a critically stressed part.

The work reported here is based on a programme of development, continuing use, and refinement of an acoustic microscope that is capable of scanning surfaces up to 46 cm × 46 cm in extent and manipulating parts as heavy as 100 kg. The broadband ultrasonic system is capable of transmitting and receiving acoustic pulses at centre frequencies from 0.5 to 100 MHz with an overall usable bandwidth from 50 kHz to 200 MHz. The large bandwidth is necessary because of the broadband pulses. Operating in several frequency ranges, it requires less than 60 s to change both the transducer and operating frequency from 0.5 to 100 MHz. This system is in its fifth year of operation, having produced its first image in April 1980; it has been operating for over a year in the considerably refined form shown in figure 1. At this time it can acquire, process, display, and store both planar and three-dimensional images of up to 30 megabytes, by using either gated amplitude or waveform capture as the image data base.

To approve a part for service, on the basis of a scanned ultrasonic evaluation, the material volume and surface must be inspected with scanned acoustic fields that cover (insonify) the part to a specified uniformity. The depths of field must be sufficient to interrogate the volume in a single scan, or additional scans must be positioned so that their overlap does not result in a gap in detection probability. Finally, the sensitivity at which the part is evaluated must be established by the critical flaw size. The following discussion will treat these requirements for surfaces, volumes, and specific interior planes (such as attachment interfaces) under separate headings.

PHILOSOPHICAL TRANSACTIONS OF THE ROYAL SOCIETY A MATHEMATICAL, PHYSICAL & ENGINEERING SCIENCES

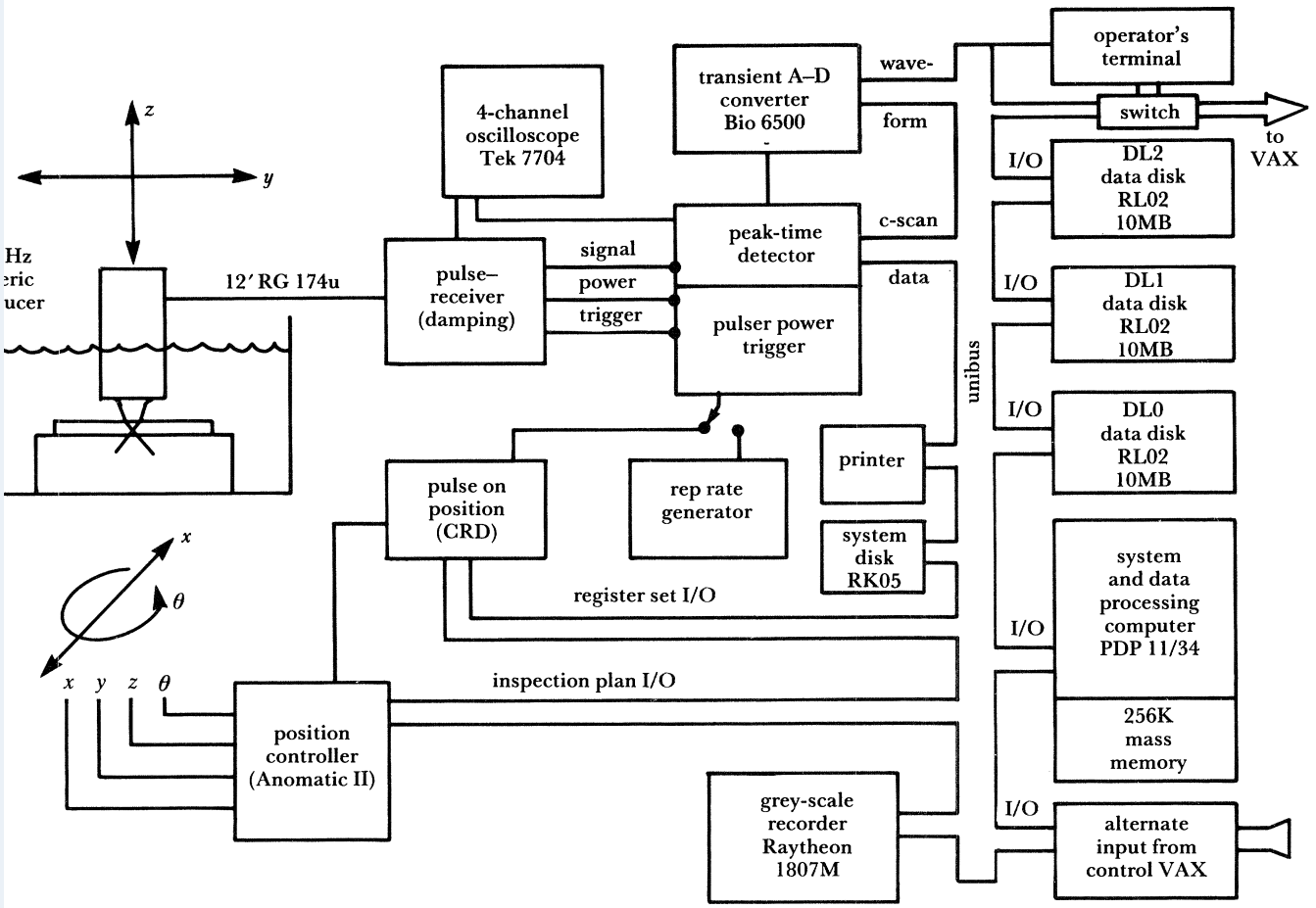

FIGURE 1. Schematic of computer-assisted microscope.

2. DESCRIPTION AND THEORY OF MEASUREMENT

(a) *Inspection of surfaces*

A considerable body of work has been directed toward the use of acoustic microscopes to image the surface of solids: for example, in the study of integrated circuits (Miller 1982) and in the investigation of grain size in metals (Briggs *et al.* 1982; Somekh *et al.* 1984). Most of these studies have operated relatively narrow bandwidth microscopes at frequencies in the range of 0.75–2.0 GHz and in the reflection mode. In the integrated circuit work, it is generally accepted that the primary contrast mechanism is due to the sensitivity to height variations of the microscope's output voltage. When flat micropolished metallurgical specimens are scanned to determine their grain size, the primary contrast mechanism is due to the sensitivity of the microscope's output voltage to the grain-to-grain changes in the material surface-wave velocity. Considerable effort has been expended to separate the effects of surface position from the effects caused by the physical properties of the surface material (Bertoni 1984). An additional effort has been needed to explain quantitatively the effect that variations in the amplitude and the phase of these separate arrivals have on output voltage. Since the patterns derived from both *surface position* and *material properties* are very similar and are received over

the same time interval by these narrowband microscopes, it has been difficult to separate these two effects reliably.

The broadband technique used in this work allows the separation of the surface-wave arrival from the unwanted direct reflection (figure 2*a*) by simply time resolving the surface wave. This is accomplished by first generating the acoustic signal with an ultrasonic transducer critically damped to a bandwidth equal to 100% of its carrier frequency. Focused by a high-index acoustic lens, in this case silicon, the system needs to be defocused only enough to separate clearly the surface-wave arrival time from that of the direct reflection. The surface wave can then be gated directly, and the variation in its amplitude used to generate the image.

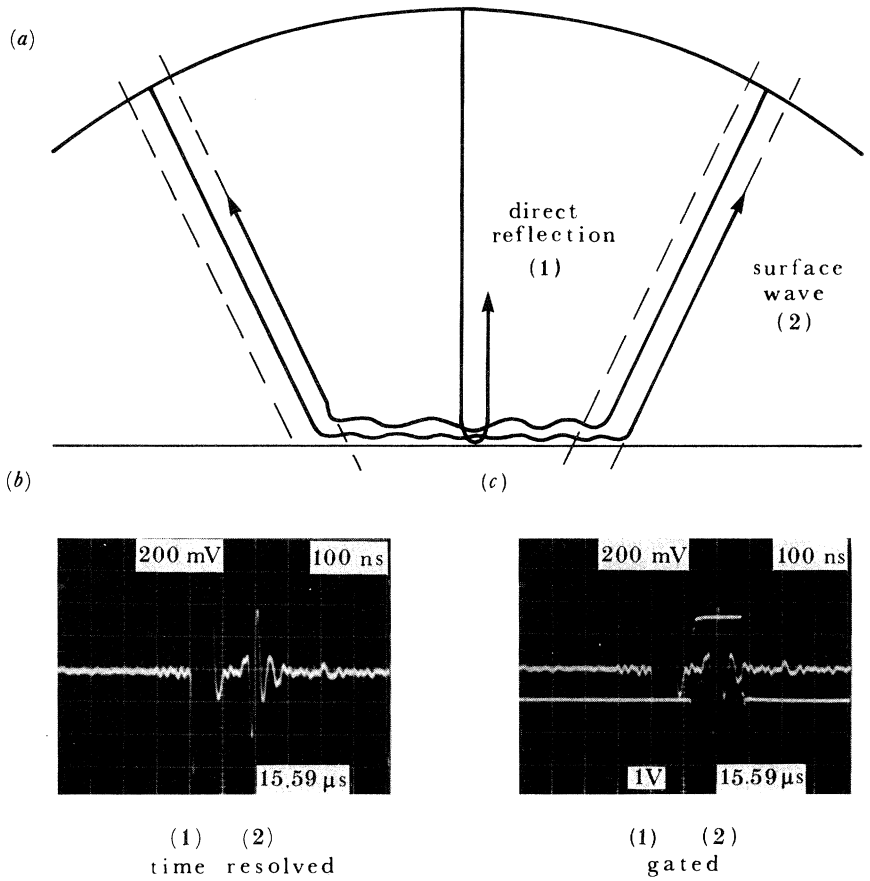

FIGURE 2. Time domain display of surface-wave signals resolved from direct surface reflection.

The time domain displays (figure 2*b*, *c*) show a 30 MHz surface wave arrival generated on the surface of an aircraft engine superalloy plate by a broadband 50 MHz acoustic pulse. The beam is defocused so that the arrival trails the direct reflection by 160 ns. Since the directly reflected pulse is only 80 ns in duration, that is the minimum required to resolve the surface wave. The 160 ns interval is used only for clarity. The loss of the higher-frequency components in the surface-wave arrival is due partly to material attenuation, partly to losses into the water, and partly to the spatial distribution of the annular region on the surface over which the surface waves are generated. In this discussion the surface distribution of the perimeter of the entry circle will be ignored, and the source of Rayleigh waves will be treated as a line source with

a radius of curvature equal to the circle diameter resulting from the Rayleigh incident-angle cone with the flat entry surface.

In isolating the surface wave from the direct reflection, with respect to the mechanisms that form the surface-wave images, the reflection microscope has now been transformed into a transmission microscope (figure 3). Each ray proceeds from the piezoelectric element (1) to

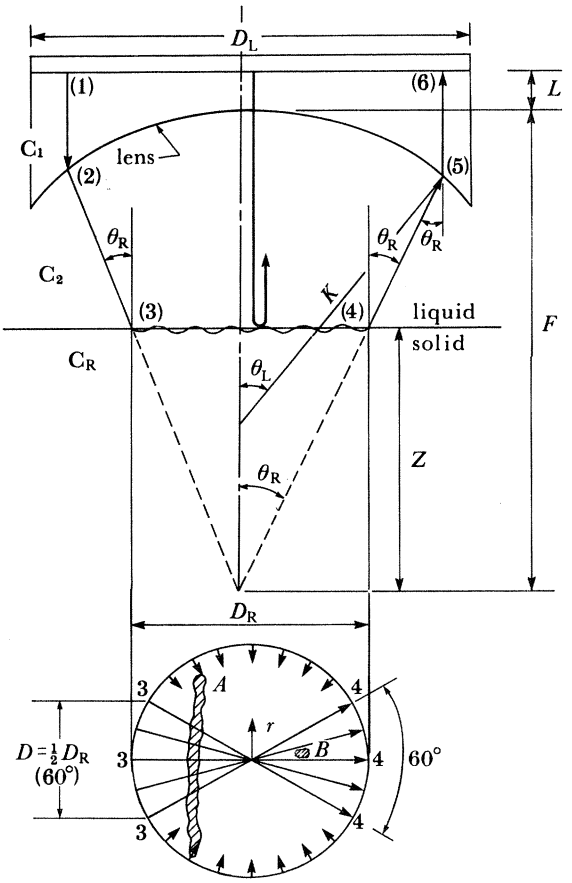

FIGURE 3. Diagram of entry circle of surface wave showing the pulse-transmission nature of the received signals and a 60° segment from the 360° convergence of the rays.

the lens (2); those which are refracted at the Rayleigh critical angle (θ_R) proceed in a converging cone of rays to intersect the specimen surface (3), where they form an entry circle of diameter D_R. They then mode convert to surface waves and propagate across the specimen on a circle diameter to the far side (4) where they reconvert and proceed back to the piezoelectric element, (5) and (6). For a buffer rod of length L, a lens or radius K, focusing at an axial distance F, and defocusing at axial distance Z, the time required for the ray on the lens axis to travel from the piezoelectric element to the sample surface and return is

$$t_1 = 2L/C_1 + 2(F-Z)/C_2, \tag{1}$$

where C_1 and C_2 are the velocity in the lens and coupling fluid, respectively. The round-trip travel time for the ray incident at the Rayleigh critical angle is

$$t_2 = \frac{2L}{C_1} + \frac{2K(1-\cos\theta_L)}{C_1} + \frac{2(F-Z)-2K(1-\cos\theta_L)}{C_2\cos\theta_R} + \frac{2Z\tan\theta_R}{C_R}, \tag{2}$$

where θ_L, θ_R, and C_R are the lens angle, the Rayleigh angle, and the Rayleigh velocity, respectively. The diameter (D_R) of the entry circle on which the incident ray is converted to a Rayleigh wave is

$$D_R = 2Z \tan \theta_R \tag{3}$$

and

$$\theta_R = \arcsin (C_2/C_R). \tag{4}$$

The time interval between the direct surface reflection and the pulse travelling across the surface is determined by subtracting (1) from (2) to give

$$t_2 - t_1 = \frac{2K(1-\cos\theta_L)}{C_1} + \frac{2(F-Z)-2K(1-\cos\theta_L)}{C_2 \cos\theta_R} + \frac{2Z\tan\theta_R}{C_R} - \frac{2(F-Z)}{C_2}. \tag{5}$$

For a given signal pulse length set equal to $t_2 - t_1$ and a lens material velocity, (5) can be solved for the required defocus $(F-Z)$.

Any discontinuities on the specimen surface that block, change direction, or change the amplitude of any of the converging bundle of surface-wave rays will change the amplitude received by the piezoelectric element. The mechanism by which this occurs can be clarified by considering two opposing 60° segments of the entry circle in figure 3, and again to consider only those rays propagating from left to right. The 60° segment clearly depicts a cylindrically converging ray bundle, point focused at the centre of the entry circle and then diverging to the opposite side of the circle perimeter. What is, in fact, displayed is a surface-wave transmission acoustic microscope that is focused by the curvature of the entry surface circle. If the circle is scanned from left to right over a target, A, whose spatial extent exceeds the beam, then, to a first approximation, the target will block or partly block the surface waves as long as it is included in the entry circle. As target B passes through the circle, it will block fewer rays until it reaches the centre. There the number of rays blocked depends on the ratio of the diameter of B to the diameter of the diffraction limited focal spot formed by the convergent surface wave. If both A and B are acoustically similar with respect to their partial reflectance and transmission of surface waves, and B exceeds the spot size in the centre, then both will cause about the same peak–trough drop in amplitude as they pass from circle left, through circle centre, to circle right. Target A, however, will produce a large amplitude decrease over the full circle diameter, whereas target B will produce a smaller decrease, except when it is located at the centre.

The 360° convergence of the rays from the periphery of the entry circle, combined with the pulse-transmission nature of the time-resolved surface-wave signal, will produce the same drop in amplitude for a crack-like discontinuity at any surface breaking orientation. It can detect any surface crack, at equal detection probability, *independent of orientation*. The capability to detect such flaws from any orientation is a significant breakthrough in ultrasonic testing, which for the past four decades has been considered one of the *least* dependable methods of interrogating surfaces because of the failure to detect cracks at certain orientations. This new capability is particularly important for highly stressed surfaces such as steam-turbine rotor bores and the bores of aircraft engine discs. This observation of the detection improvement can be shown from the work on cracks by Yamanaka & Enomoto (1982).

The two parameters describing the resolution of the time-resolved, surface-wave imaging system illustrated in figure 3 are the diameter of the entry circle (D_R) and the spot size of the surface-wave focal zone at the centre of the circle. The spot diameter (d_{sc}) can be calculated

PHILOSOPHICAL TRANSACTIONS OF THE ROYAL SOCIETY A MATHEMATICAL, PHYSICAL & ENGINEERING SCIENCES

from the amplitude point spread function of the double cylindrical lens system placed on the entry surface by the entry circle. The point spread function has been shown (Born & Wolf 1975) to be of the form

$$H(X) = \mathrm{sinc}^2 X, \tag{6}$$

where $X = (2Dr)/(\lambda_R D_R)$, λ_R is the Rayleigh wavelength in the solid, r is the distance from the image point, D_R/Z is the radius of the entry circle, D is the chord length of the 60° arc segment of the entry circle, and $\mathrm{sinc}\, X = \sin(\pi X)/(\pi X)$. Kino (1980) has suggested (figure 4) that a simple resolution criterion would be the width of the central maximum of $H(X)$ at the -3 dB points. For $\mathrm{sinc}^2 X$ this would occur at

$$d_{sc} = 2r = 0.64\lambda_R D_R/2D. \tag{7}$$

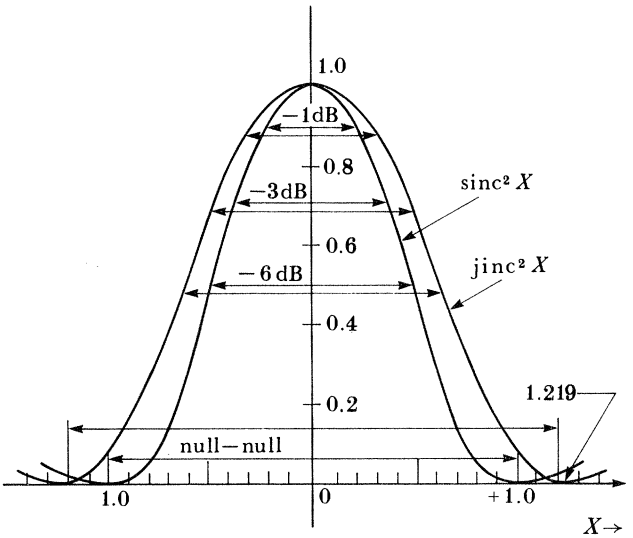

FIGURE 4. Diagram of the main lobes of $\mathrm{sinc}^2 X$ and $\mathrm{jinc}^2 X$ showing the -1, -3, and -6 dB as well as null-to-null diameters.

Equation (7) evaluated for the 60° segment of the entry circle of diameter D_R, where $D = \frac{1}{2}D_R$ gives

$$d_{sc} = 0.64\lambda_R. \tag{8}$$

In order to extend this analysis to the entire entry circle, it is only necessary to recognize that there are three 60° segments transmitting from right to left and three transmitting from left to right, and that all are received by the piezoelectric element and added algebraically. For the entire circle $D = D_R$ and $Z = \frac{1}{2}D_R$ and the -3 dB resolution spot size formed in the centre of the entry circle by all rays from 360° becomes, for $Z/D = 0.5$,

$$d_{sc} = 0.32\lambda_R. \tag{9}$$

Because this indicates that a discontinuity slightly less than one third of a surface wavelength in linear extent can conceivably cause a -3 dB change in amplitude, (9) explains the consistently surprising resolution of this method and of all surface-wave imaging techniques that involve the formation of an entry circle and that develop the cylindrically convergent surface wave.

The compound resolution of this system may now be evaluated quantitatively. The entry surface circle must be at least two or three wavelengths in diameter in order to time resolve the surface-wave arrival; so D_R is at least ten times the diameter of the spot size at its centre. Cracks, seams, and other linear discontinuities having little width but with lengths L that exceed D_R are imaged as having a width that approaches D_R and a length that approaches $L+D_R$.

Small discontinuities, however, will produce a significant amplitude decrease only when they interact with the zone of focus at the centre; however, they will produce lower level decreases in amplitude as soon as they become included in the entry circle. For any position in the entry circle, a small equiaxed discontinuity of diameter d_R (flaw B in figure 3) produces an amplitude change in proportion to the ratio of number of surface wave rays that intersect the discontinuity to the total number of rays in the circle. The number of intersected rays drops significantly as the position of the discontinuity moves from the centre, where it intersects all of the rays, to the periphery. If A_{max} is the drop in amplitude produced by the discontinuity at the centre, and if the number of rays blocked are assumed to increase linearly as a small flaw ($0 < d_f < D_f$) is scanned towards the centre of the entry circle, by inspection of figure 3 the amplitude ratio (A_p/A_{max}) for any position in the circle for $0 < r < \frac{1}{2}D_R$ is

$$\frac{A_p}{A_{max}} = \frac{d_f}{D_f}\left(1 - \left|\frac{2r}{D_R}\right|\right), \tag{10}$$

where D_R is again the entry circle diameter and d_f, D_f, and r are the diameter of the discontinuity, the diameter of a beam-blocking discontinuity, and the distance from the circle centre at which A_p is being calculated, respectively.

Figure 5 shows the amplitude response against flaw position from (10). The largest possible amplitude decrease (A_{max}) is a function of the size D_f, as well as the acoustic properties of the discontinuity. If d_f is smaller than the overall diameter of the centre spot, then it will block proportionately less of the acoustic signal. Clearly the minimum diameter of a totally blocking flaw determines the size required to produce a maximum signal drop at circle centre. If this

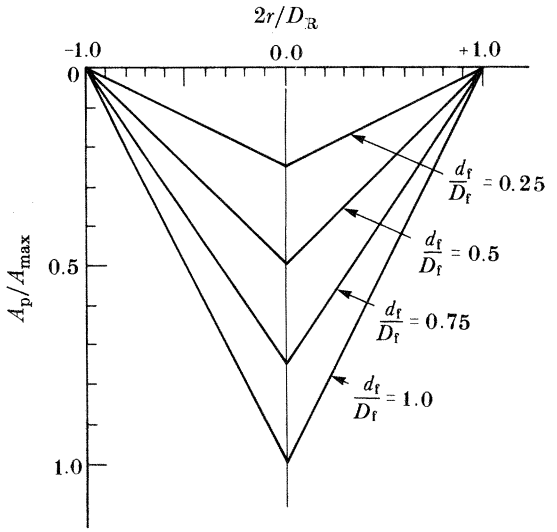

FIGURE 5. Proportionate amplitude drop in received surface wave signal resulting from rays being blocked by a flaw of diameter d_f, where D_f is equal to the beam diameter.

is taken as the null points on either side of sinc X, figure 4, then for a distance of $Z = \frac{1}{2}D_R$ and a lens diameter of D_R, the flaw diameter D_f that will block the entire beam for $Z/D = 0.5$ is the null–null diameter for sinc X or

$$D_f = 2.0\lambda_R\, D_R/2D_R = 1.0\lambda_R, \tag{11}$$

where λ_R is again the Rayleigh wavelength.

In the specification of a scan plan, it is necessary to use the appropriate spot dimension for the line–line spacing and the pulse–pulse spacing along the line. If the interrogating acoustic field is to be scanned to the uniformity of a single shade of grey (−3 dB), then both the lines and the pulses can be spaced at $0.32\lambda_R$. If the scanned acoustic field is to be uniform to −1 dB, then both spacings must be reduced to $0.16\lambda_R$. The −1 dB spacing is very close to one half the −3 dB spacing. For the 50 MHz surface-wave images discussed in §3*a*, λ_R for both the glass and the steel samples is within 3%, and the $0.16\lambda_R$ spacing for all of the images is 0.05 mm.

(*b*) *Inspection of volumes*

Although normally a near-surface instrument (Atalar 1985), the acoustic microscope can also be used to inspect volumes. The critical reflecting-flaw size to be detected is the key design parameter that establishes the sensitivity for the non-destructive evaluation of a volume of material. This flaw (figure 6) must block a sufficient fraction of the focused beam so that a

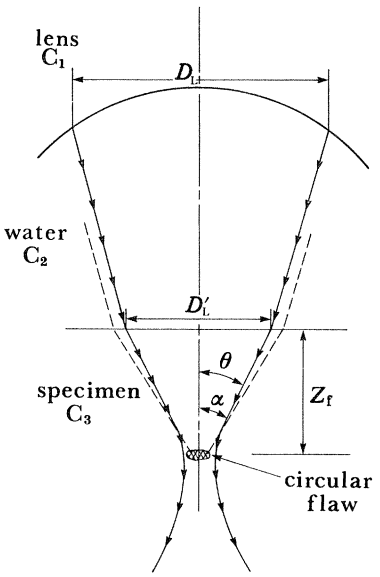

FIGURE 6. Geometry of beam-blocking flaw for volume scan.

detectable signal is reflected back to the transducer. The detectable size can be expressed as a fraction of the beam area or a fraction of the minimum reflector size that reflects the same amplitude back to the transducer that would be reflected by an infinite surface. Once detected, a flaw may be characterized, with respect to its size and shape, by an additional, much higher resolution beam.

In cases of substantial coherent acoustic noise from the focal zone, an alternative specification

PHILOSOPHICAL TRANSACTIONS OF THE ROYAL SOCIETY A MATHEMATICAL, PHYSICAL & ENGINEERING SCIENCES

would be to specify the detectable flaw in terms of the ratio of its reflected amplitude to that of the noise. The detectable amplitude is usually given as two, three, or four times the root mean squared noise depending on the permissible false-alarm ratio. This amplitude can then be evaluated with respect to the detectable flaw size. In this case the design engineer must either approve or disapprove the test with respect to its noise-limited detection capability.

Volume inspection also requires that an acoustic field be scanned to a uniform amplitude throughout its length, width, and depth. In order for this to be accomplished in an economical number of scans, the interrogating beam must have a depth of field (or length of focus) that is, if not equal to, at least an appreciable fraction of the material depth. For many industrial parts this could be 1–10 cm or considerably greater. If the material is to be scanned to a uniformity of −1 dB, peak-to-peak, then the −1 dB diameter and the −1 dB depth of focus must again be established for the interrogating acoustic beam. For very small flaws there may be no economical solution. A beam diameter small enough to detect the flaws may require too much time to complete a scan of the material volume.

The first concern, however, is to make sure that the critical flaw is detected. If a reflecting flaw is smaller than the focused beam, then the reflected amplitude is in proportion to the ratio of the area of the flaw to the area of the beam (Krautkramer & Krautkramer 1977). As a first approximation, the shape of the flaw cross section may be assumed circular if it is totally contained in the beam. For detection purposes, therefore, the size of the beam area may be taken as the area required to block the beam. A circular reflecting disc of diameter D_f, perpendicular to and centred on the axis of symmetry of a focused acoustic beam, will totally block the beam if the back-reflected beam angle from the disc is equal to the angle of convergence of the focused beam. If λ_3 is the wavelength incident on the disc, then, as shown in figure 6, the back-reflected beam half angle (Hueter & Bolt 1955) may be calculated:

$$\sin\alpha = 1.2\lambda_3/D_f. \tag{12}$$

The half angle of the convergent acoustic field produced by a focusing lens of diameter D_L and focal length Z is specified by

$$\sin\theta = \tfrac{1}{2}D'_L/[(D'_L/2)^2+Z^2]^{\frac{1}{2}}. \tag{13}$$

Setting (12) equal to (13) and solving for D_f gives

$$D_f = 2.4\lambda_3[(\tfrac{1}{2}D'_L)^2+Z^2]^{\frac{1}{2}}/D'_L. \tag{14}$$

For $Z > D'_L$, the approximation

$$D_f = 2.4\lambda_3 Z/D'_L \tag{15}$$

is quite accurate. It will be explained later in this section why (15), by using the focus and wavelength in water, will specify the blocking flaw for most given transducer–lens combinations.

The insonification by the focused beam across the face of disc D_f does not have the uniformity assumed in the derivation of (15). In practice, however (Krautkramer & Krautkramer 1977), measurements of the reflected amplitude from flat-bottomed holes with diameters equal to D_f, usually fall within a few decibels of the infinite surface amplitude as measured from a flat backwall reflection. Therefore (15) does give a practical blocking diameter.

For a normally incident pulse–echo beam (figure 7) focused by an axially symmetric lens

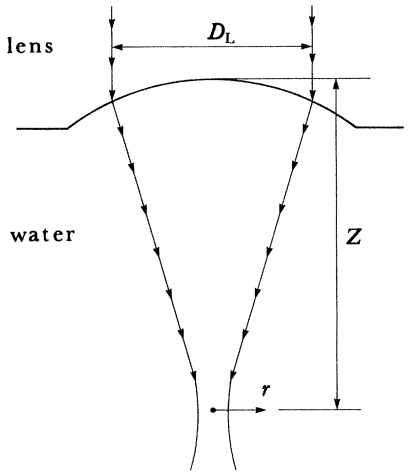

FIGURE 7. Geometry of beam for point-spread function calculation.

with a circular margin, the point spread function (Born & Wolf 1975; Kino 1980; Monk 1937) shown in figure 4 is

$$H(X) = \text{jinc}^2 X, \tag{16}$$

where again $X = D_L r/\lambda_2 Z$, λ_2 is the wavelength in the focusing medium (water), r is the distance from the image point in the focal plane, $\text{jinc}\, X = J_1(\pi X)/(\pi X)$, $J_1(\pi X)$ is a first-order Bessel function of the first kind, and Z is the distance from the plane of the lens to the plane of focus. The null-to-null diameter of $\text{jinc}^2 X$ (figure 4) is

$$d_{\max} = 2.4\lambda_2 Z/D_L. \tag{17}$$

Note that $2.4\lambda_2 Z/D_L$ also describes the diameter of the D_f that was calculated from the diffracting properties of a circular flaw. The -3 dB diameter of $\text{jinc}\, X$ is

$$d_{sc} = 1.03\lambda_2 Z/D_L, \tag{18}$$

and the -1 dB diameter is

$$d_{sc'} = 0.5\lambda_2 Z/D. \tag{19}$$

Again it is the smallest diameter that must be used to establish the distance between scan lines and the pulse-to-pulse distance along the scan lines if the scanned field is to be uniform to -1 dB. Note that the null-to-null diameter for $\text{jinc}^2 X$ is $2.4\lambda Z/D_L$, which gives the same value for a blocking flaw D_f as (15) gave by calculating a back-reflecting angle equal to the convergent lens angle.

The amplitude as a function of depth along the axis of symmetry of a circularly focused beam is not as well understood as the point spread function, but Schlangermann (in Krautkramer & Krautkramer 1977) gives an expression that can be evaluated to give a depth of focus. Neglecting phase, the pressure distribution along the axis of symmetry of a spherically converging wave front from a focused radiator (figure 3) of diameter D_L and radius of curvature K is

$$P/P_0 = \left(\frac{2}{1-Z/K}\right)\left|\sin\left[\frac{\pi}{\lambda_2}\{[(Z-h)+\tfrac{1}{4}D_L]^{\frac{1}{2}}-Z\}\right]\right|, \tag{20}$$

PHILOSOPHICAL TRANSACTIONS OF THE ROYAL SOCIETY A MATHEMATICAL, PHYSICAL & ENGINEERING SCIENCES

where $h = K - (K - \frac{1}{4}D_L)^{\frac{1}{2}}$ and where λ_2 is the wavelength. Equation (20) is of the indeterminate form $\sin X/X$. The most convenient way to evaluate (20) is numerically, where the series of Z values used for the calculations approach, but never equal, K.

Monk (1937) has given a solution for an optical depth of focus ($l_{sc'}$) for a focal length Z and lens diameter D_L as

$$l_{sc'} = 4\lambda_2(Z/D_L)^2. \tag{21}$$

Monk's value for $l_{sc'}$ corresponds reasonably well to the -1 dB acoustic depth of field when it is compared both with the numerical evaluations of (20) and the experimental evaluation of focused broadband transducers. Equation (21) therefore forms the most convenient basis for the depth of field calculations for scanning plans.

When a focused beam is introduced into a solid material with an ultrasonic wave velocity (C_3) greater than that of water, the wavelength (λ_3) increases in accordance with the velocity ratio (C_3/C_2) and the distance (Z) to the focus decreases in accordance with the inverse velocity ratio C_2/C_3, where C_2 is the longitudinal velocity in water. Therefore, to a first approximation and neglecting aberration effects, the velocity ratios cancel and beam diameters described by (17) through (19) also describe the beam diameter in the solid. It is for this reason that the focal diameters of the transducer-lens in water can be used to calculate blocking flaws in the materials being evaluated.

The depth of focus, however, is shortened by the refraction produced at the water–solid interface so that the value for $l_{sc'}$ within the solid becomes

$$l_{sc'} = 4\lambda_2(Z/D_L)^2(C_2/C_3). \tag{22}$$

With expressions for critical flaw size, sensitivity, and $d_{sc'}$ and $l_{sc'}$, a scanning plan can now be established for the inspection volume.

(*c*) *Inspection of interior planes (bond lines)*

In the inspection of volumes, aberration effects can often be neglected because the reduced apertures (large Z/D) that are required to produce acoustic beams with large depths of field minimize aberration. However, when it is necessary to inspect a plane at high resolution and small depth of field such as a bonded interface, then it becomes both appropriate and expedient to design a transducer that focuses sharply at that depth (Jipson 1979).

Pino *et al.* (1981), using a geometric optics approach, defined an aspheric lens surface that produces a diffraction limited focus at a specified depth in a high velocity solid. Applying Fermat's principle, the transit time for all rays (figure 8) are equalized from the focus-to-plane L–L' for all values of θ from the axis of symmetry ($\theta = 0$) to that of the extreme marginal ray. By using Snell's law to establish the relation between ϕ and θ as

$$\phi = \sin^{-1}[(C_2/C_3)\sin\theta], \tag{23}$$

the equalized transit time for each ray requires

$$\frac{\Delta Z}{Z_1}\left(\frac{C_1/C_2 - \cos\phi}{C_1/C_2\cos\phi}\right) = \frac{Z_f}{(C_3/C_2)Z_1}\left(\frac{1-\cos\theta}{\cos\theta}\right) + \left(\frac{1-\cos\phi}{\cos\phi}\right), \tag{24}$$

where Z_1 and Z_f are the water path and focal depth beneath the surface of the water–solid interface, respectively. The other parameters, θ, C_1, C_2, and C_3 are the angle of the extreme

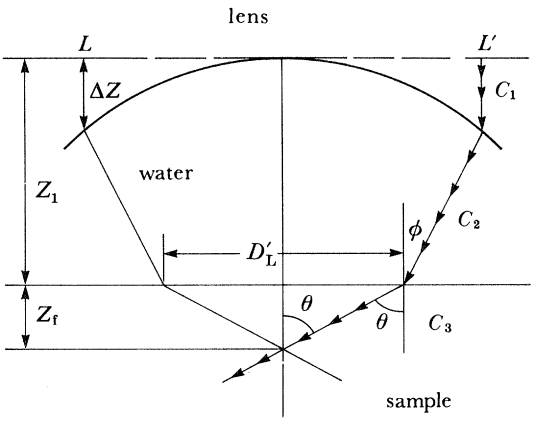

FIGURE 8. Design of aspheric lens for the interrogation of interior planes.

marginal ray at the focus, and the velocities in the lens, the coupling fluid, and the solid part, respectively.

The size of the diffraction-limited focal spot for aspherics is controlled by the point spread function given in (16). However, an aspheric lens is focused by the high-velocity material it interrogates, and no focus is formed in the fluid coupling medium. Therefore it is necessary to specify the focal zone dimensions in terms of the wavelength in medium 3, the depth at which the beam is designed to focus (Z_f), and the diameter of the entry circle, made by the marginal rays, on the fluid–solid interface ($D'_L = 2Z_f \tan\theta$). The -1 dB diameter and depth of the aspheric focal zone can now be given as

$$d_{sc'} = 0.5\lambda_3\, 1/2 \tan\theta \tag{25}$$

and

$$l_{sc'} = 4\lambda_3\, (1/2 \tan\theta)^2, \tag{26}$$

where λ_3 is the bulk wavelength in the material. It is instructive to calculate the -1 dB depth of field for various half angle convergences in steel for a 50 MHz ($\lambda_3 = 0.12$ mm) aspheric beam. The diameter and depth of focus for 30° ($f/0.87$) convergence are 0.042 mm or approximately one third of a wavelength and 0.36 mm or three wavelengths, respectively. For 50° ($f/0.42$), the diameter and depth are 0.02 and 0.08 mm or $\frac{1}{6}$ and $\frac{2}{3}$ wavelength, respectively.

TABLE 1. RESOLUTION SPOT SIZE (d_{sc}) AND DEPTH OF FOCUS FOR INCREASING Z/D

Z/D	θ/deg	$d_{sc'}/\lambda$	$l_{sc'}/\lambda$
0.5	45.00	0.2	1
1.0	26.56	0.4	4
2.0	14.04	0.8	16
3.0	9.46	1.2	36
4.0	7.13	1.6	64
5.0	5.71	2.0	100
6.0	4.76	2.4	144
7.0	4.09	2.8	196
8.0	3.56	3.2	256
9.0	3.18	3.6	324
10.0	2.86	4.0	400

PHILOSOPHICAL TRANSACTIONS OF THE ROYAL SOCIETY A MATHEMATICAL, PHYSICAL & ENGINEERING SCIENCES

It is clear from table 1 that the diffracted depth of focus rapidly converges on the diameter as the focal length to diameter ratio decreases. Table 1 holds for both spheric and aspheric beams providing that aberration can be neglected.

3. Results

The acoustic images included in this section were all originally displayed on a hard-copy grey-scale recorder with a recording width of 43.0 cm over which up to 4096 pixels may be displayed at 16 steps of grey. The dynamic range of the ultrasonic system is 8 bits of amplitude discrimination, so that the arrangement of the 16 steps of grey over the range of data is accomplished with the use of a histogram (figure 9). Two linear ramps are provided in the

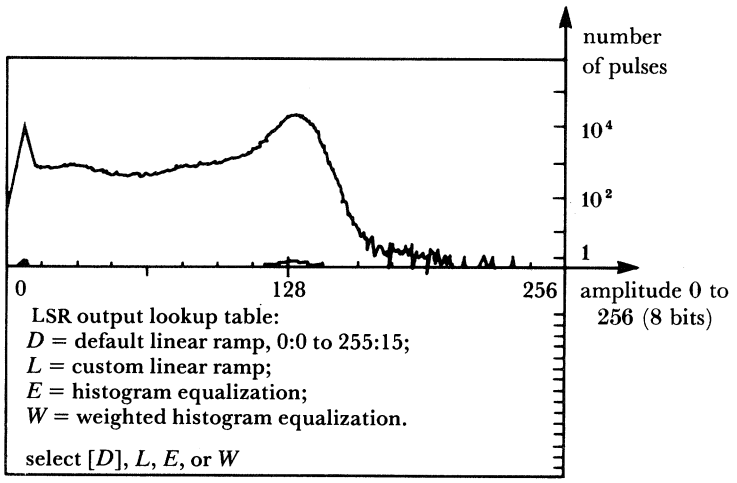

Figure 9. Histogram for figures 14, 15, and 16 showing the menu of available grey-scale ramps for the processing and display of images.

menu, and two ramps are based on a histogram algorithm. The custom linear ramp simply sets the start and finish of the ramp somewhere on the scale of 0–256. Both the histogram algorithms also are set with respect to start and finish. The equalized histogram assigns the grey-scale steps on the basis of equal numbers of acoustic pulses occurring between given amplitude ranges between the start and stop values. As the amplitudes get larger, fewer pulses are included and therefore larger increments in range are required to get the necessary $\frac{1}{16}$ for that level of grey. The weighted forward histogram assigns proportionately fewer numbers of pulses to the larger amplitudes and, therefore, provides more grey-scale definition for the larger amplitudes.

(*a*) *Inspection of surfaces*

Line-pair resolution has been the standard by which image resolution has been measured since it was originally proposed by Rayleigh. Figure 10(*a*, *b*) shows images of a line-pair resolution plate, prepared by erosion lithography of a 25.4 mm fused quartz blank. Each target on the plate is a set of three etched bars separated by two equivalent spaces of undisturbed quartz surface. The direct reflection image in figure 10*a* shows the detail of the bar patterns

PHILOSOPHICAL TRANSACTIONS OF THE ROYAL SOCIETY A MATHEMATICAL, PHYSICAL & ENGINEERING SCIENCES

PHILOSOPHICAL TRANSACTIONS OF THE ROYAL SOCIETY A MATHEMATICAL, PHYSICAL & ENGINEERING SCIENCES

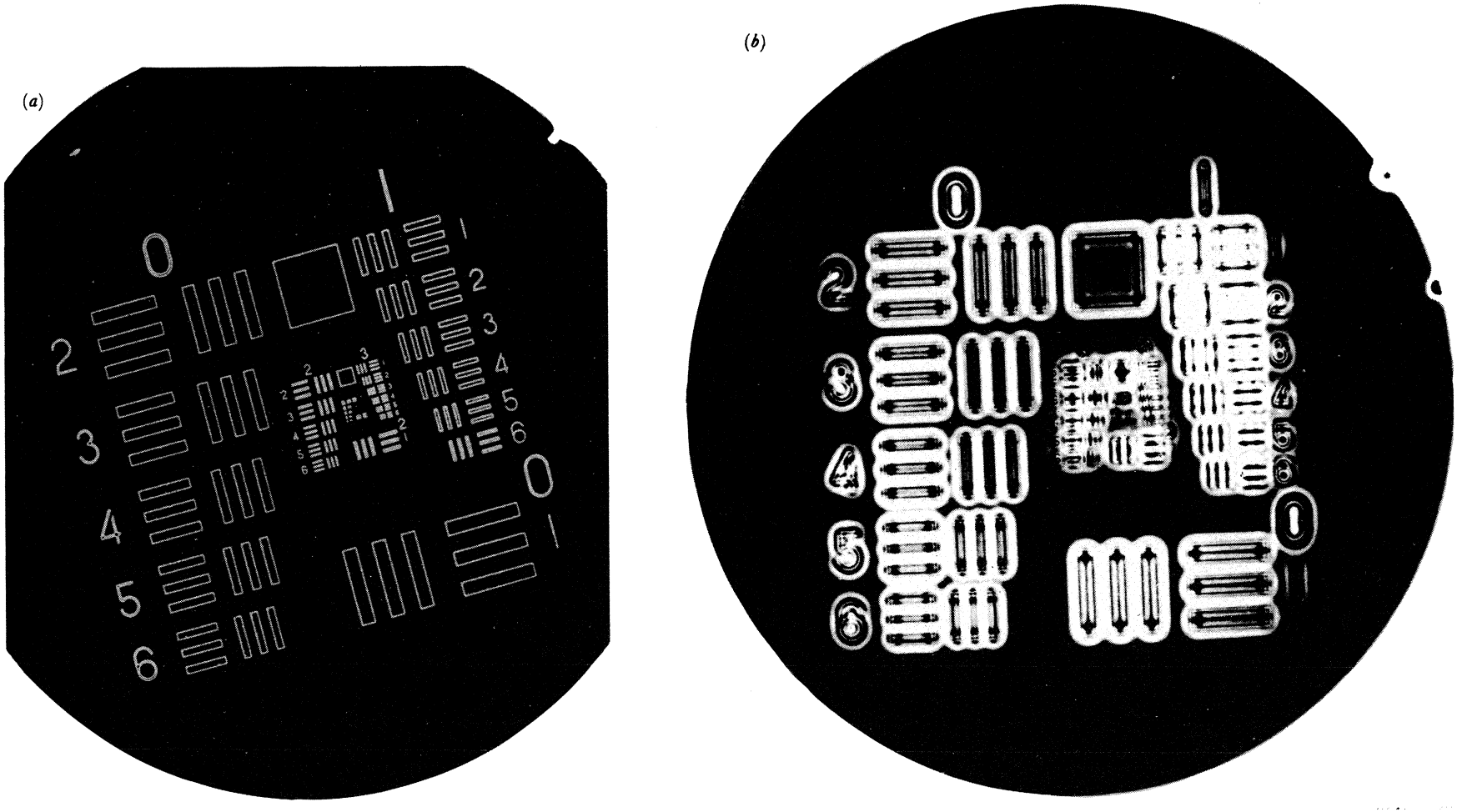

FIGURE 10. Fused quartz IC resolution plate having an overall circular diameter of 25.4 mm. Patterns are etched into glass surface with erosion lithography, $C_R = 3.48$ mm/μs, $d_{sc} = 0.04$ mm. Patterns are five sets (0, 1, 2, 3, 4) of bar-space combinations of equal width, each set one-half of the previous in size. The largest of set 0 is 0.8 mm; the largest of set 4 (not resolved in surface wave or direct reflection image) is 0.05 mm. (*a*) Direct reflection image with plate in transducer focal plane, (*b*) surface-wave image, $D_R = 0.86$ mm; 50 MHz transducer, 6.0 mm in diameter focused at 4.8 mm in water; −3 dB focal spot size in water is 25 μm.

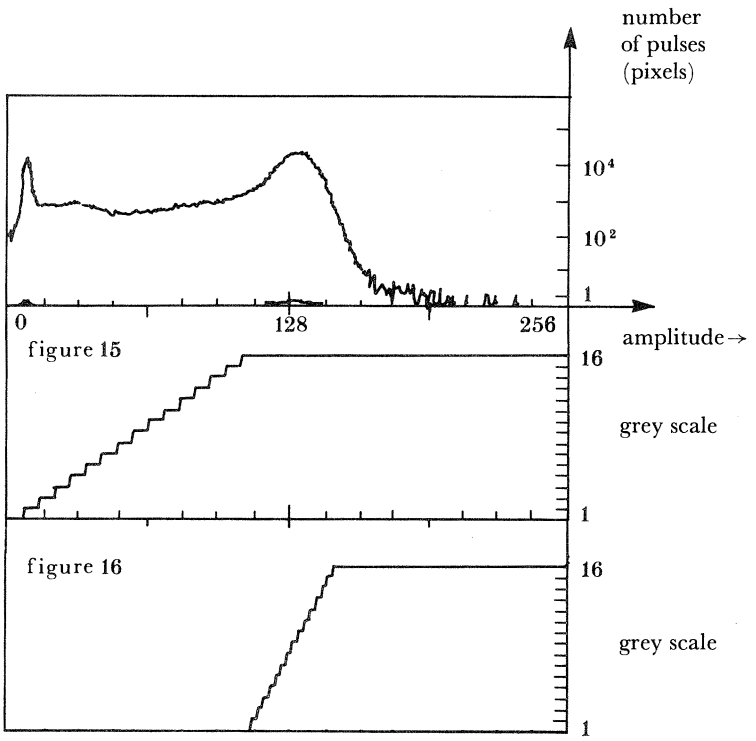

FIGURE 14. Histogram and grey scales for figures 15 and 16; linear ramps are used to display the images.

on the plate to a −3 dB resolution of 25 μm. Note that the principal sources of contrast are the edges of the bars. Because of the stepped-down nature of the surface at the bar locations, they tend to form small resonant cavities for the trapped surface-wave signal, resulting in the interference maxima shown. The period of the gated surface-wave signal was 38 ns, indicating a carrier frequency for the pulse of 26.1 MHz. This should indicate a −3 dB spot size between 0.04 and 0.05 mm. It is difficult to convince an objective observer, however, that targets less than 0.1 mm can be resolved even at magnifications of 20 times. The white halos around all of the line pair sets show a dimensional correspondence to the bar size that was not expected. It appears to be due to the smaller patterns being less deeply cut, and therefore blocking less of the surface wave, even although they exceed the entry circle diameter.

Figures 11–13, plates 1 and 2, show acoustic scans on a mild steel sample composed of eight segments that are soldered together. The first purpose of the sample design was to provide a test block to demonstrate that the convergent surface wave could detect long linear surface-breaking flaws or seams regardless of orientation. The uniformity with which the eight seams are imaged at both of the entry circle diameters does demonstrate omnidirectional detection. A second purpose was to demonstrate that the apparent width of the crack was in fact due to the entry circle diameter but that smaller targets could also be imaged. Note that the periodicity of the contrast on the surfaces of the 45° wedges are very similar in figures 11 and 12. This similarity indicates that the microstructure interacts primarily with the zone of focus at the centre of the entry circle and that this zone remains much the same diameter in spite of the large entry circle change. Figure 13 is displayed at approximately four and a half times the magnification of figures 11 and 12. It provides much clearer detail on the interaction

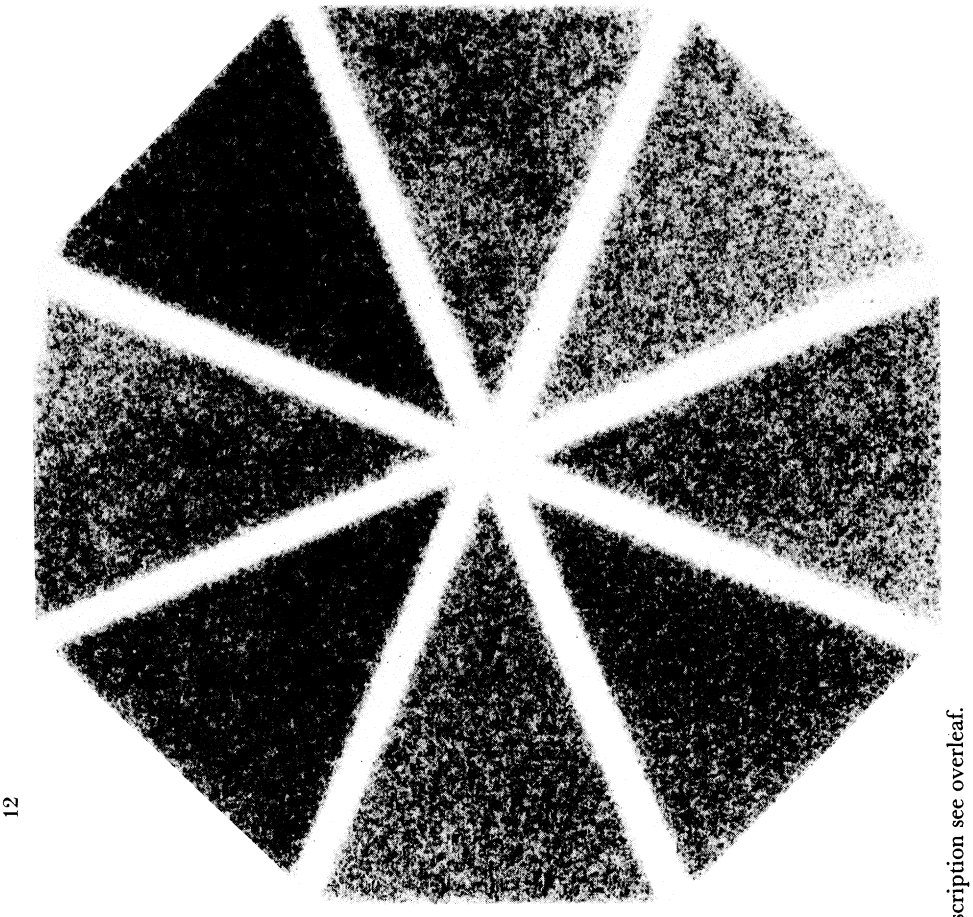

12

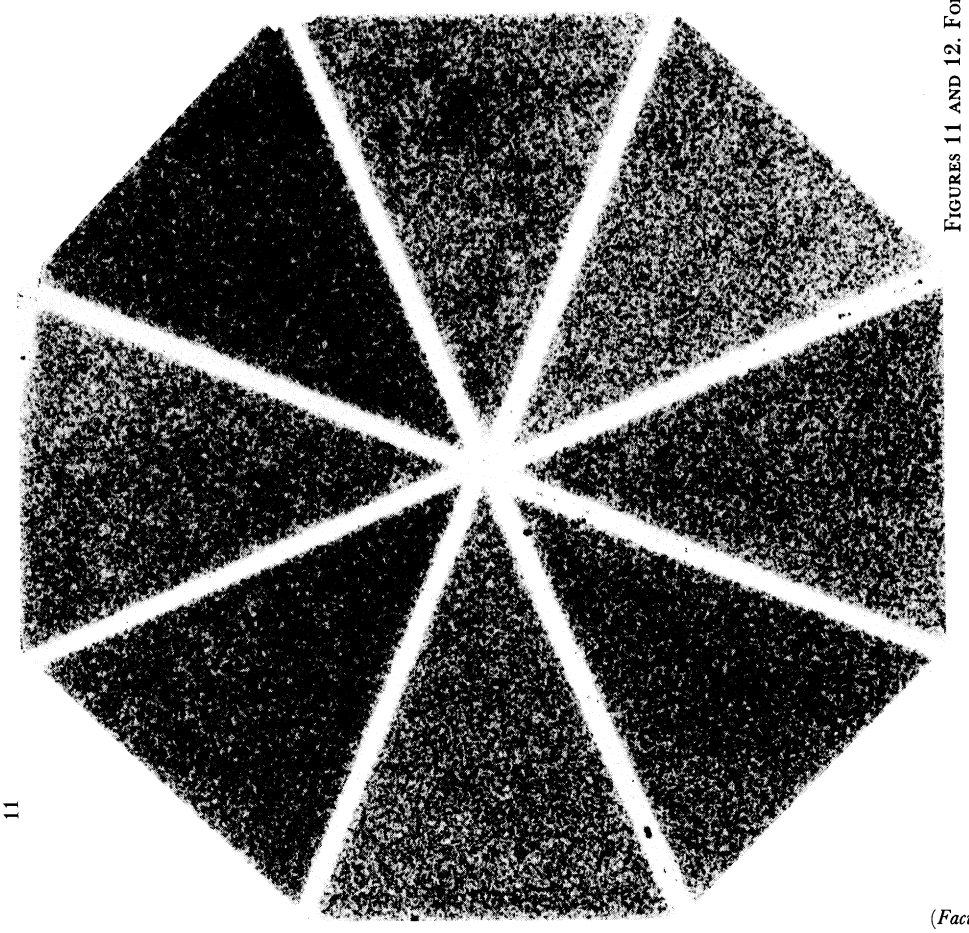

11

FIGURES 11 AND 12. For description see overleaf.

PHILOSOPHICAL TRANSACTIONS OF THE ROYAL SOCIETY A MATHEMATICAL, PHYSICAL & ENGINEERING SCIENCES

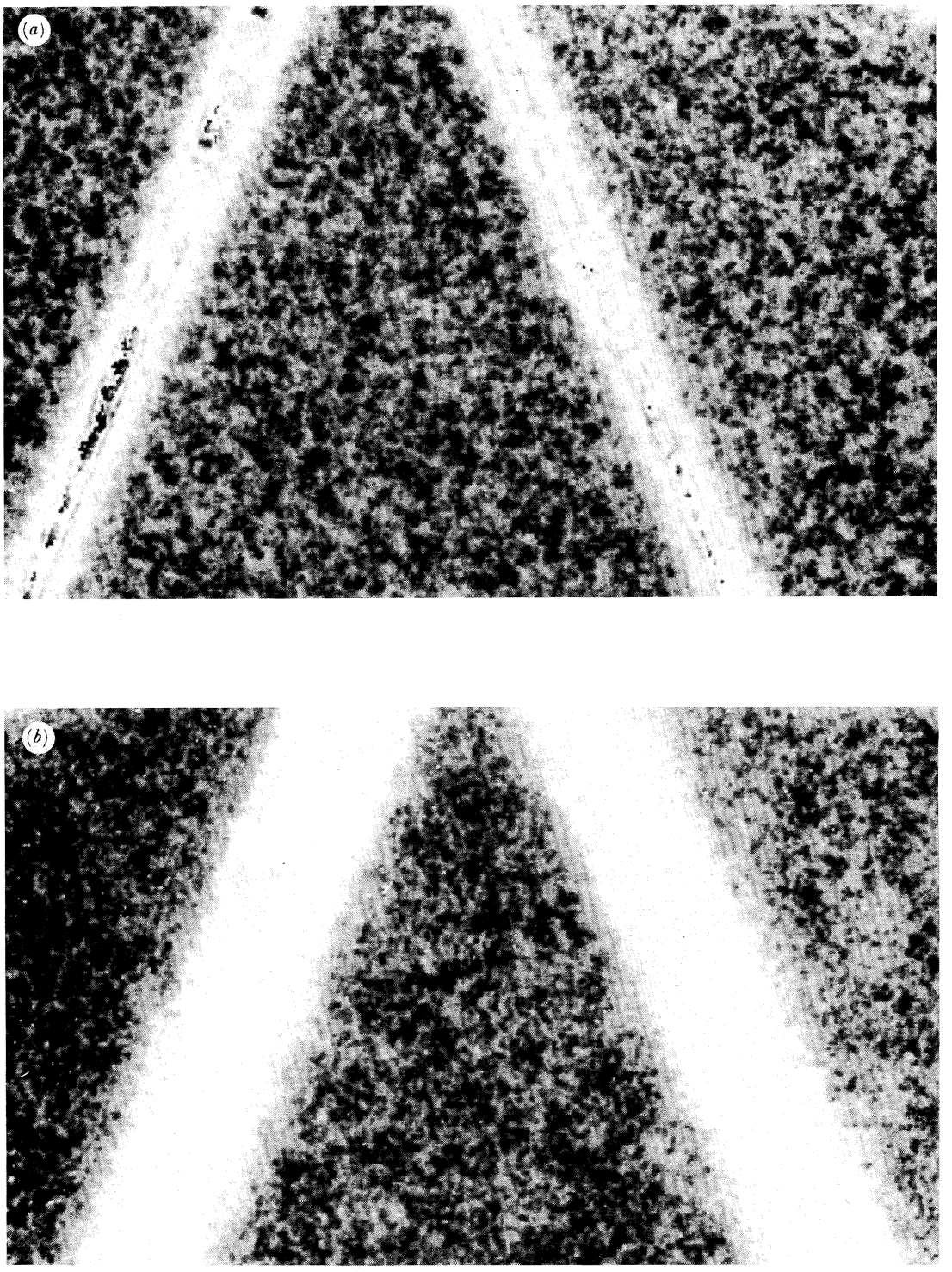

FIGURE 13. An enlarged view of the apex of the central lower segment of (*a*) figure 11 and (*b*) figure 12.

DESCRIPTION OF PLATE 1

FIGURE 11. Mild steel sample composed of eight segments soldered together, $C_R = 3.04$ mm μs^{-1} in steel; 50 MHz transducer, 6.0 mm in diameter focused at 4.8 mm in water, $D_R = 0.6$ mm; sample is 35.7 mm, flat-to-flat.

FIGURE 12. Same as figure 11, except $D_R = 1.1$ mm.

PHILOSOPHICAL TRANSACTIONS OF THE ROYAL SOCIETY A MATHEMATICAL, PHYSICAL & ENGINEERING SCIENCES

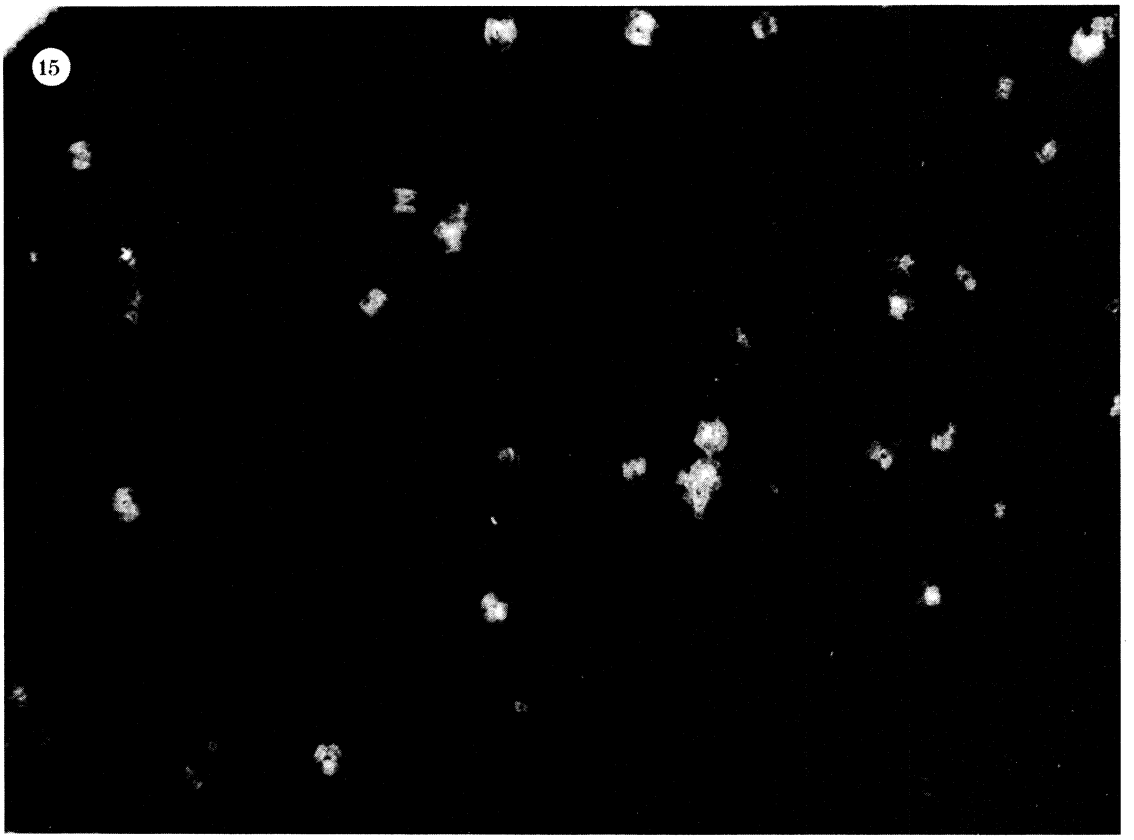

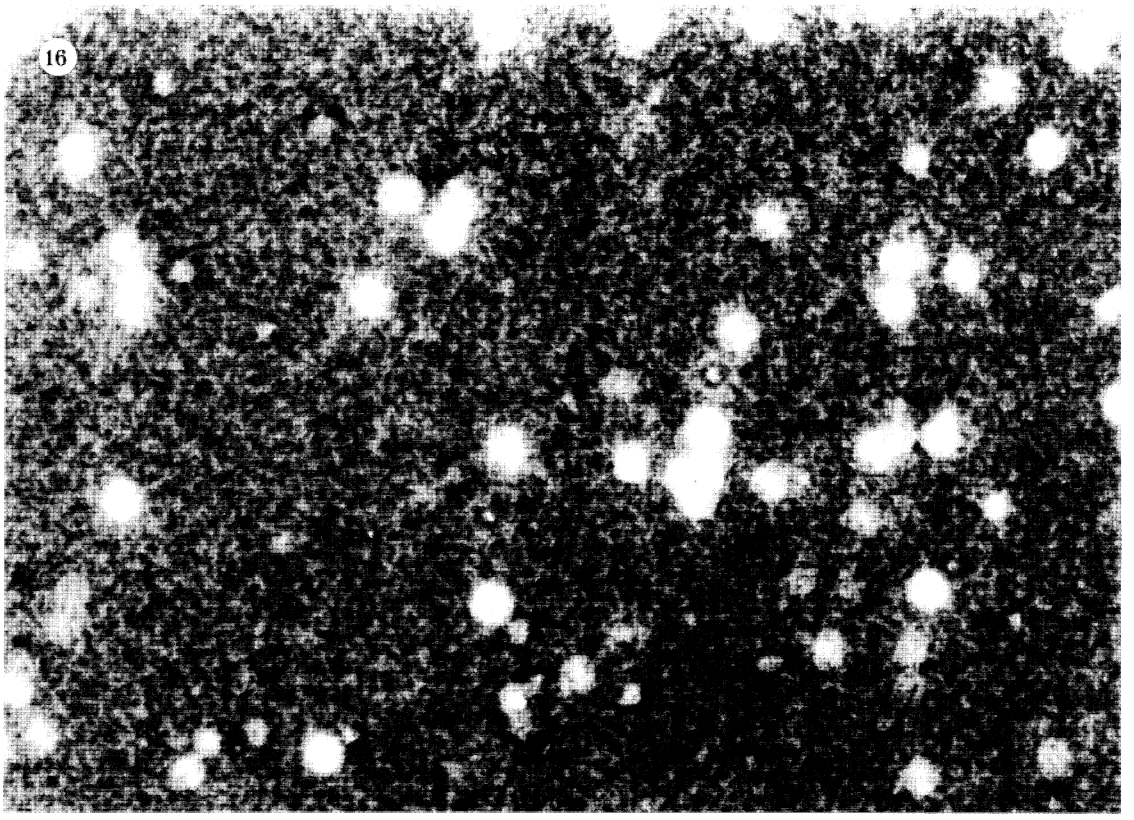

FIGURE 15. Hot isostatically pressed sample of an aircraft engine superalloy (René 95) with 0.1–0.15 mm alumina fragments sintered in the metal. Grey scale set to show only surface-breaking flaws. $C_R = 3.175$ mm μs^{-1}, $D_R = 0.46$ mm; 50 MHz transducer, 6.0 mm in diameter focused at 4.6 mm in water. Sample size is 12.5 mm × 15.62 mm.

FIGURE 16. Same data file as figure 15, except grey scale now set to show detail of microstructure.

PHILOSOPHICAL TRANSACTIONS OF THE ROYAL SOCIETY A MATHEMATICAL, PHYSICAL & ENGINEERING SCIENCES

PHILOSOPHICAL TRANSACTIONS OF THE ROYAL SOCIETY A MATHEMATICAL, PHYSICAL & ENGINEERING SCIENCES

21

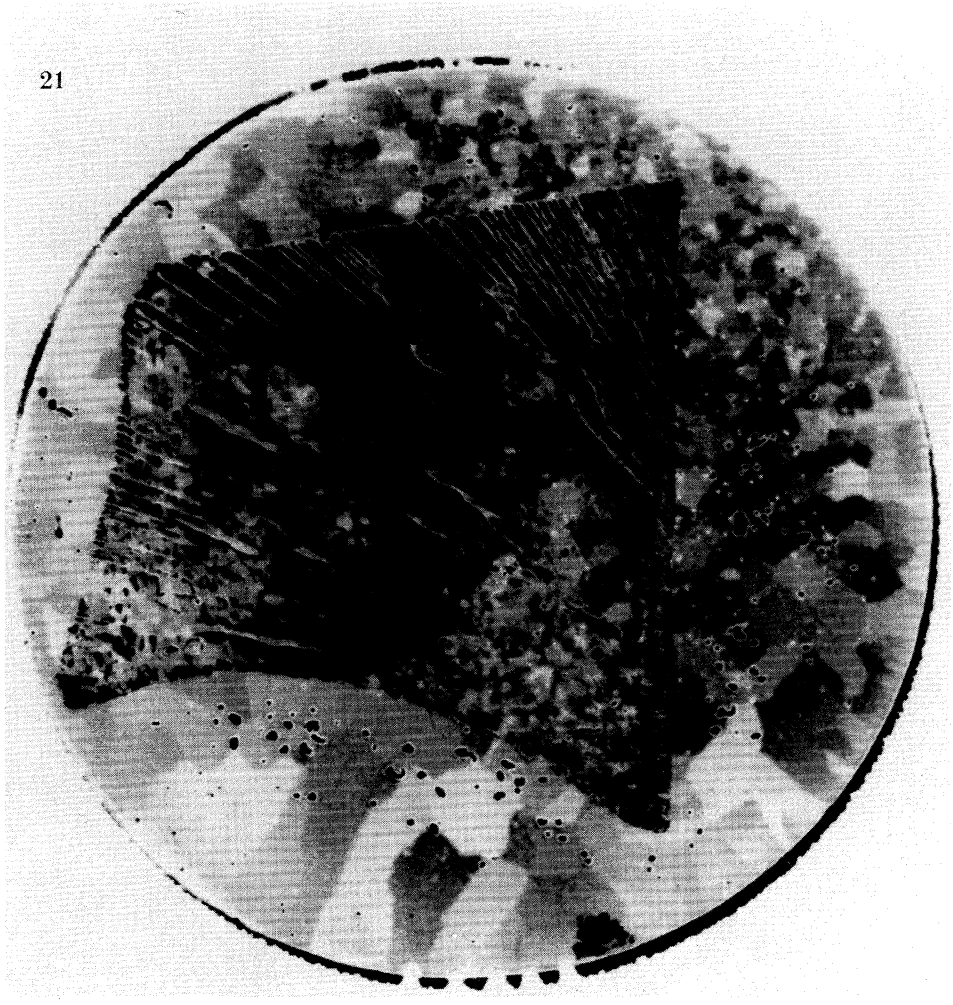

22

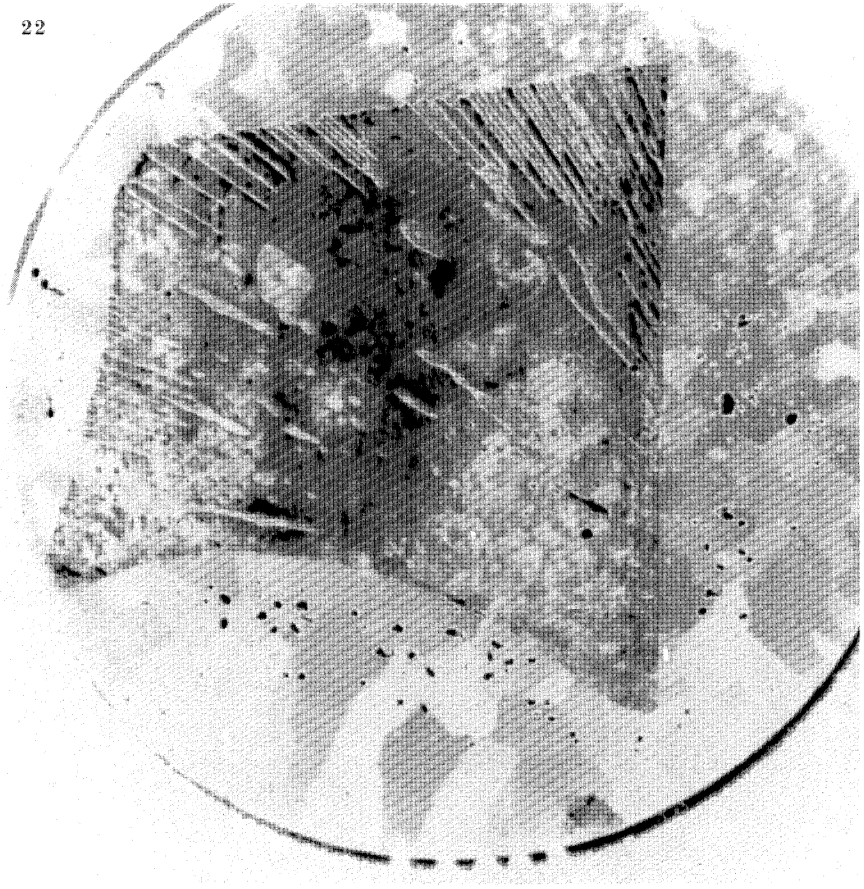

FIGURE 21. Image of solder bond-layer between two 43.0 mm silicon discs, each 0.5 mm thick. Layer was formed by melting a 0.025 mm solder foil (black outline) in a vacuum. Grey scale for figure 21 is a linear ramp adjusted to emphasize the grain size distribution in the intact portion of the solder layer. Voids and grains are readily apparent.

FIGURE 22. Image from same data set as figure 21. Grey scale is set by an equalized histogram algorithm, which, in this case, permits the voids and other signals of equal amplitude to be separated clearly from the remaining structure.

between the focal spot and the microstructure, and, although the periodicity of the microstructure does remain much the same, attenuation from the larger entry circle has somewhat washed out the image.

One of the clear advantages of the compound resolution of the time-resolved surface-wave signal is the ability to monitor both major flaws and microstructure simultaneously. Figure 14 shows two grey-scale ramps, set to display only major flaws (figure 15) and then set to display the effect of the microstructure on the surface-wave signal (figure 16).

Figure 14 and figures 15 and 16, plate 3, show a 12.50 mm × 15.62 mm René 95 sample that contains alumina fragments sintered into the metal matrix. This sample was prepared to demonstrate the high detectability of inclusions at the surface and near the surface. Note that even when the grey scale is displayed so that the signal from the unbroken surface is flat black, the inclusions display a somewhat diffuse edge. This is due to the gradient in ray intersections encountered by the small targets as they are scanned from the periphery through the centre of the entry circle.

Although the large difference in acoustic impedance restricts images formed from the direct surface reflection of solid objects to contain only surface morphology, these images can give considerable detail on the condition of the surface. Figure 17 shows an example of such detail on a circulated Canadian penny in addition to providing a qualitative example of the resolution spot size of the same 50 MHz transducer used for figures 10–16.

FIGURE 17. (*a*) Direct reflection image from obverse surface of Canadian penny; same 50 MHz transducer as figure 14, $d_{sc} = 0.025$ mm. (*b*) Reverse face of coin. The penny is 19 mm in diameter.

(*b*) *Inspection of volumes*

In the inspection of surfaces or interior planes, the constraints are somewhat different from the inspection of volumes. In volume inspection there is an additional dimensional tradeoff between resolution and inspection time that is inverse to the resolution spot size squared. By doubling the spot size, the depth of field is quadrupled. Therefore, in addition to the reduction in scan lines, there is twice that reduction in the volume inspection time. A comparison of

PHILOSOPHICAL TRANSACTIONS OF THE ROYAL SOCIETY A MATHEMATICAL, PHYSICAL & ENGINEERING SCIENCES

figures 18 and 19 clearly shows this. Each of the René 95 calibration blocks was machined from the same piece of as-pressed material. The block shown in figure 18 was scanned with a 6.0 mm diameter, 50 MHz, $\frac{1}{2}f$ transducer focused at 12.5 mm in water. In order to limit aberration, the focal depth in the metal was limited to 1.5 mm. The image shown in figure 19 was scanned with a transducer of identical design except it is focused at 19.0 mm in water ($\frac{1}{3}f$). Both

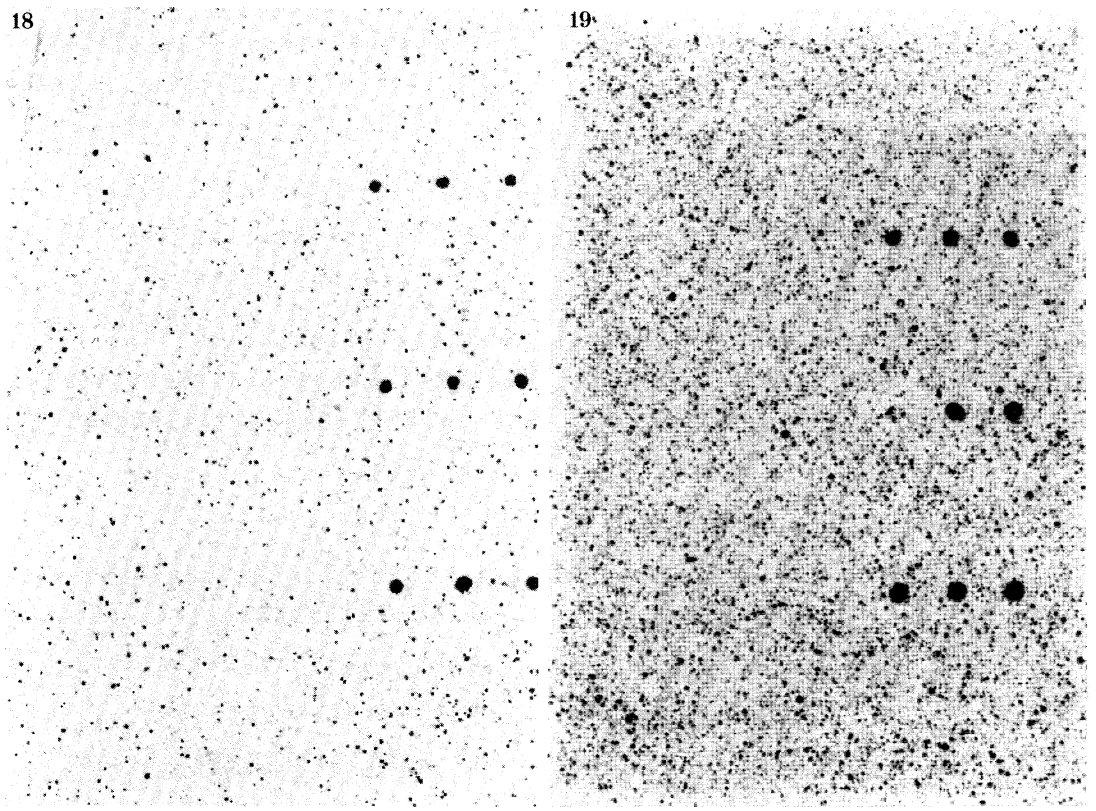

FIGURE 18. As-pressed sample of René 95 from 150 mesh powder showing 0.25, 0.375, and 0.5 mm electrodischarge machined holes and porosity, $C_L = 6.04$ mm μs^{-1}; 50 MHz transducer, 6.0 mm inn diameter focused at 12.5 mm in water, $d_{sc} = 0.06$ mm, $l_{sc'} = 0.12$ mm; plane of focus and ends of holes are both 1.5 mm deep. Sample size is 24.0 mm × 35.0 mm × 3.1 mm.

FIGURE 19. As-pressed sample of René 95 as in figure 18 but with dimensions of 24.0 mm × 35.0 mm × 6.3 mm. Plane of focus and end of holes are 3.1 mm deep; 50 MHz transducer, 6.0 mm in diameter focused to 19.0 mm in water, $d_{sc} = 0.091$ mm, $l_{sc'} = 0.27$ mm. Note the larger number of detected pores resulting from the greater depth of field.

transducers easily showed the machined targets; the missing target in figure 19 is due to a machining error. However, figure 19 shows twice the number of indications at only slightly less resolution. Because the metal specimen in figure 18 contains the same level of porosity as the specimen scanned for figure 19 with the deeper focus transducer, the difference in the two images is due largely to the difference in depth of field of the two transducers.

(*c*) *Inspection of interior planes* (*bond lines*)

Figure 20 shows a histogram of the scanning data on a solder attachment layer bonding two pieces of silicon together. The first grey scale configuration is a linear ramp, set to show the

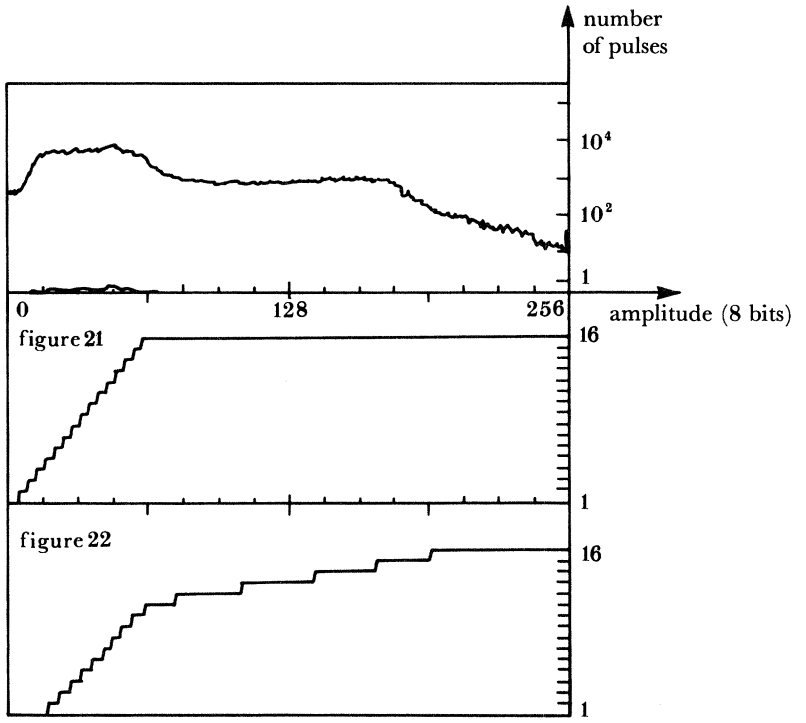

FIGURE 20. Histogram of data forming figures 21 and 22, showing arrangement of grey-scale ramps used to display the image.

grain size in the intact solder layer. The second grey scale is set by a histogram equalization algorithm, over the full range of the data on the silicon, but displaced from the origin to avoid including the large number of acoustic pulses that fell off the silicon disc.

The data set was taken with a 50 MHz aspheric lens designed to focus sharply in silicon at a depth of 0.125 mm. Because the thickness of each silicon disc is 0.4 mm, the beam at the solder layer was defocused approximately the difference in depth less half of the depth of field.

The specimen was fabricated in a two-step process. Initially two silicon wafers were placed in a low-temperature vacuum furnace with a piece of solder foil between them. During the combined evacuation, melting and out-gassing, the bubble tracks were formed. The specimen was then cooled under vacuum and removed. At this stage, it was inspected with X-ray, and large voids were found in the solder layer. It was then reheated under atmospheric pressure to drive the solder into the evacuated voids. At this stage in its fabrication it was scanned, and the images shown in figures 21 and 22, plate 4, are the result of that scan.

The linear ramp image (figure 21) shows large portions of the disc to be apparently unbonded, or of at least equivalent amplitude to the portions of the image that can be identified as voids. It should be noted that the original large voids are now filled with solder. The histogram image (figure 22) shows that only the largest of the voids and only a portion of the area of the original solder foil fragment appear at the highest reflected amplitude. The advantage to the second display method is that it shows the microstructure and yet still allows differentiation between levels of poor bonding.

PHILOSOPHICAL TRANSACTIONS OF THE ROYAL SOCIETY A MATHEMATICAL, PHYSICAL & ENGINEERING SCIENCES

4. Conclusions

Ultrasonic c-scan images for materials evaluation were first produced three decades ago (Buchanan 1955). During the last decade, the sophistication and usability of c-scan imaging have vastly improved, largely because of the progress made in acoustic microscopy. However, materials evaluation for industrial purposes and materials characterization for the metallurgist or materials engineer involve a difference of twelve orders of magnitude in the interrogated material volume.

This discussion has been directed toward adapting acoustic microscopy techniques to industrial problems. The results, particularly in the evaluation of near surface material, have been very rewarding. The broadband surface-wave method introduced in this discussion should be of particular interest to those investigators who must evaluate surfaces and near-surface material for performance at high temperatures and stresses.

References

Atalar, A. 1985 Penetration depth of the scanning acoustic microscope. *IEEE Trans. Sonics Ultrasonics*. **SU-32**, 164–167.

Bennet, A. & Ash, E. A. 1980 In *Scanned image microscopy* (ed. E. A. Ash), pp. 23–85. London: Academic Press.

Bertoni, H. L. 1984 Ray-optical evaluation of $V(z)$ in the reflection acoustic microscope. *IEEE Trans. Sonics Ultrasonics* **SU-31**, 105–116.

Bertoni, H. L. & Tamir, T. 1973 Unified theory of Rayleigh-angle phenomena for acoustic beams at liquid–solid interfaces. *Appl. phys. Lett.* **2**, 157.

Born, M. & Wolf, E. 1980 In *Principles of optics*. 6th Ed. London: Pergamon.

Briggs, G. A. D., Ilett, C. & Somekh, M. G. 1982 Acoustic microscopy for materials studies. In *Acoustic imaging* (ed. E. A. Ash & C. R. Hill), vol. 12, pp. 89–100. London: Plenum Press.

Bucanan, R. W. & Hastings, C. H. 1955 Ultrasonic flaw plotting equipment: a new concept for industrial inspection. *Nondestructive testing* **13**, 17.

Hueter, T. F. & Bolt, R. H. 1955 In *Sonics*, pp. 61–75. New York: John Wiley & Sons.

Jipson, V. B. 1979 Acoustic microscopy of interior planes. *Appl. phys. Lett.* **35**, 385–387.

Kino, G. S. 1980 Fundamentals of scanning systems. In *Scanned image microscopy* (ed. E. A. Ash). London: Academic Press.

Krautkramer, J. & Krautkramer, H. 1977 *Ultrasonic testing of materials*, pp. 75–79. Springer-Verlag.

Lemons, R. A. & Quate, C. F. 1974 Integrated circuits as viewed with an acoustic microscope. *Appl. phys. Lett.* **25**, 251–253.

Lemons, R. A. & Quate, C. F. 1973 Acoustic microscopy by mechanical scanning. *Appl. phys. Lett.* **24**, 165–167.

Liang, K. K., Kino, G. S. & Khuri-Yakub, B. T. 1985*a* Material characterization by the inversion of $V(z)$. *IEEE Trans. Sonics and Ultrasonics*. **SU-32**, 213–224.

Liang, K., Bennett, S. D., Khuri-Yakub, B. T. & Kino, G. S. 1985*b* Precise phase measurements with the acoustic microscope. *IEEE Trans. Sonics Ultrasonics*. **SU-32**, 266–273.

Miller, A. J. 1982 Application of acoustic microscopy in the semiconductor industry. In *Acoustic imaging* (ed. E. A. Ash & C. R. Hill), vol. 12, pp. 67–78. London: Plenum Press.

Monk, G. S. 1937 *Light, principles and experiments*. New York: McGraw-Hill.

Nikoonahad, M., Yue, G. & Ash, E. A. 1985 Pulse compression acoustic microscopy using SAW filters. *IEEE Trans. Sonics Ultrasonics*. **SU-32**, 152–163.

Parmon, W. & Bertoni, H. L. 1979 Ray interpretation of the material signature in the acoustic microscope. *Electron. Lett.* **11**, 684–686.

Pino, F., Sinclair, D. A. & Ash, E. A. 1981 New technique for subsurface imaging using scanning acoustic microscopy. *Proc. Ultrasonics Int.* **81**, 193–198.

Quate, C. F., Atalar, A. & Wickramasinghe, H. K. 1979 Acoustic microscopy with mechanical scanning – a review. *Proc. IEEE Acoustic Imaging* **67**, 1092–1113.

Saad, A., Bertoni, H. L. & Tamir, T. 1974 Beam scattering by nonuniform leaky wave structures. *Proc. IEEE* SAW Devices **62**, 1552–1561.

Sheppard, C. J. R. & Wilson, T. 1981 Effects of high angles of convergence on $V(z)$ in the scanning acoustic microscope. *Appl. phys. Lett.* **38**, 858–859.

PHILOSOPHICAL TRANSACTIONS OF THE ROYAL SOCIETY A MATHEMATICAL, PHYSICAL & ENGINEERING SCIENCES

Smith, I. R., Wickramasinghe, H. K., Farnell, G. W. & Jen, C. K. 1983 Confocal surface acoustic wave microscopy. *Appl. phys. Lett.* **42**, 411–413.
Sokoloff, S. 1950 *Uspeckhi Fiz. Nauk* (U.S.S.R.).
Somekh, M. G., Briggs, G. A. D. & Ilett, C. 1984 The effect of elastic anisotropy on contrast in the scanning acoustic microscope. *Phil. Mag.* **49A**, 179–204.
Weglein, R. D. 1985 Acoustic micro-metrology. *IEEE Trans. Sonics Ultrasonics.* **SU-32**, 255–235.
Weglein, R. D. & Wilson, R. G. 1978 Characteristic materials signatures by acoustic microscopy. *Electron. Lett.* **14**, 352–354.
Wickramasinghe, H. K. 1978 Contrast in reflection acoustic microscopy. *Electron Lett.* **14**, 305.
Yamanaka, K. & Enomoto, Y. 1982 Observations of surface cracks with scanning acoustic microscope. *J. appl. Phys.* **53**, 846–850.

Discussion

E. Almond (*National Physics Laboratory, Teddington, Middlesex, U.K.*). Dr Gilmore talked about turbine blades. These have very curved surfaces. How does this affect the way he examines the specimen?

R. S. Gilmore. Turbine blades do have very curved surfaces and are often the standard example for complex surface inspections. Curvature, however, is relative and for surface-wave inspection, the radius of curvature of the surface must be compared with D_R, the diameter of the surface-wave entry circle. If the acoustic axis of the lens is normal to a convex cylindrically curved surface with radius (k_s), the curvature would cause a decrease in the entry-surface angle equal to $D_R/2k_s$ rad. For the conical beam to achieve Rayleigh incidence in the direction of curvature, an approximate increase in the surface-wave path is required equal to $D_R Z/2k_s$, where Z is the defocus distance from figure 3. This changes the entry circle to an entry ellipse with minor and major axes of D_R and $D_R + D_R Z/2K_s$, respectively. An acceptable image will be produced only if the quality $D_R Z/2K_s$ is negligible or less than one eighth of the carrier frequency wavelength. In the case of varying curvature it is best to choose an entry-circle diameter such that the sharpest curvature produces a negligible $D_R Z/2K_s$. For broadband surface-wave inspections, typical minimum entry-circle diameters (D_R) vary from 3 to 6 surface wavelengths. A good approximation for Z is $\frac{1}{2}D_R$. If the corresponding sharpest curvatures were 30–60 wavelengths, then the ellipse axes would be D_R and 1.02 D_R, respectively and the difference 0.06–0.12 wavelengths. At 50 MHz the surface wavelength for typical turbine blade materials is 0.05 mm for steels and 0.1 mm for ceramics. At 30–60 wavelengths this would permit inspections of surfaces with radii of curvature of 1.5–3.0 mm in steel and 3.0–6.0 mm in ceramics. Such curvatures would cover all sections of most blades except at the leading and trailing edges. It might be possible to inspect the leading and trailing edges but elliptical lenses would be required to compensate for the surface curvature, and frequencies in excess of 50 MHz would be required to improve the spatial resolution and, therefore, reduce the size of D_R.

PHILOSOPHICAL TRANSACTIONS OF THE ROYAL SOCIETY A MATHEMATICAL, PHYSICAL & ENGINEERING SCIENCES

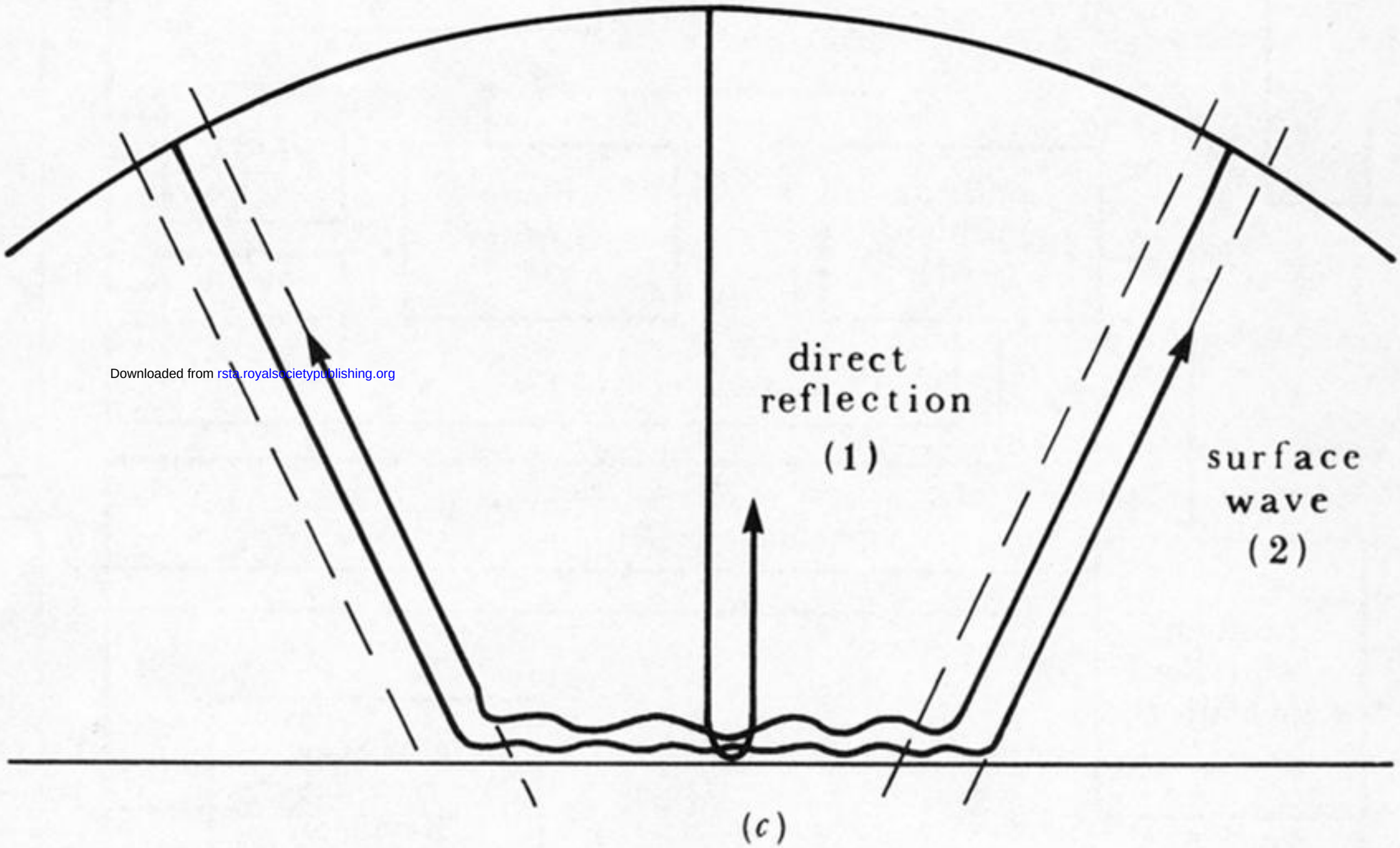

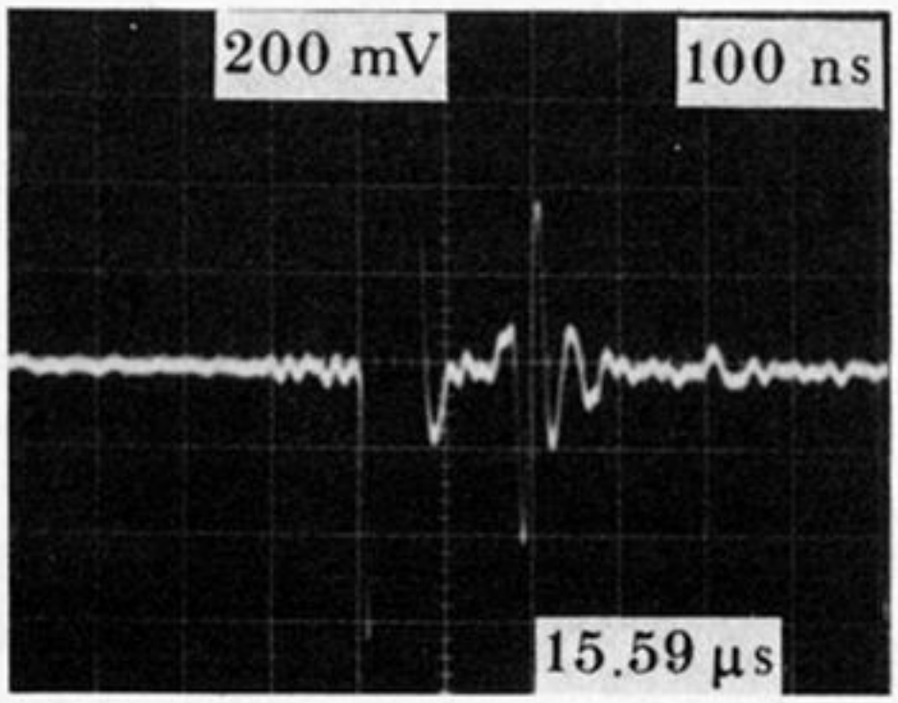

(1) (2)
time resolved

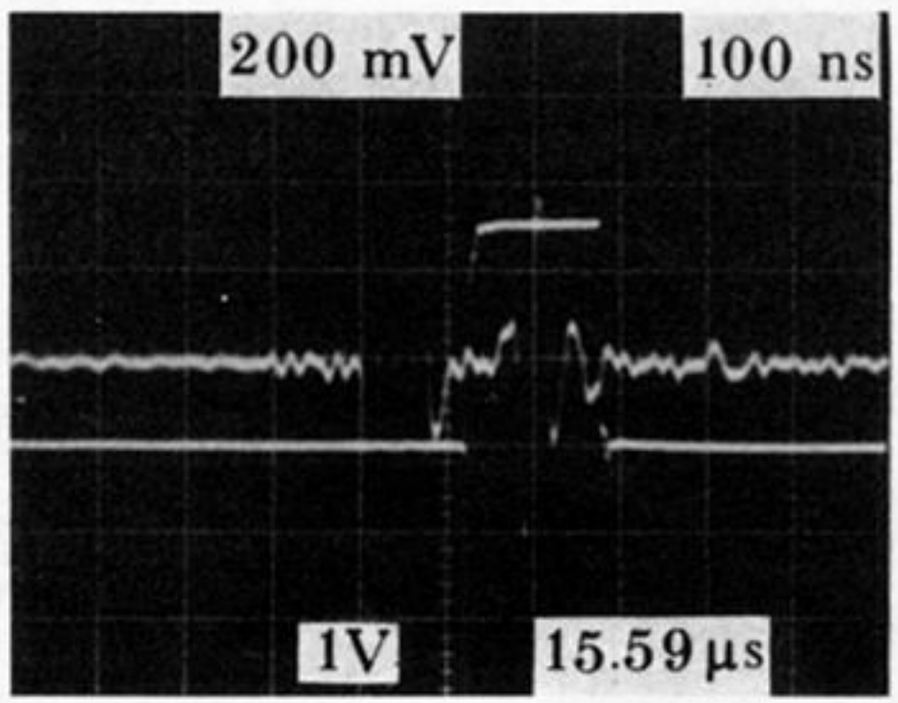

(1) (2)
gated

IGURE 2. Time domain display of surface-wave signals resolved from direct surface reflection.

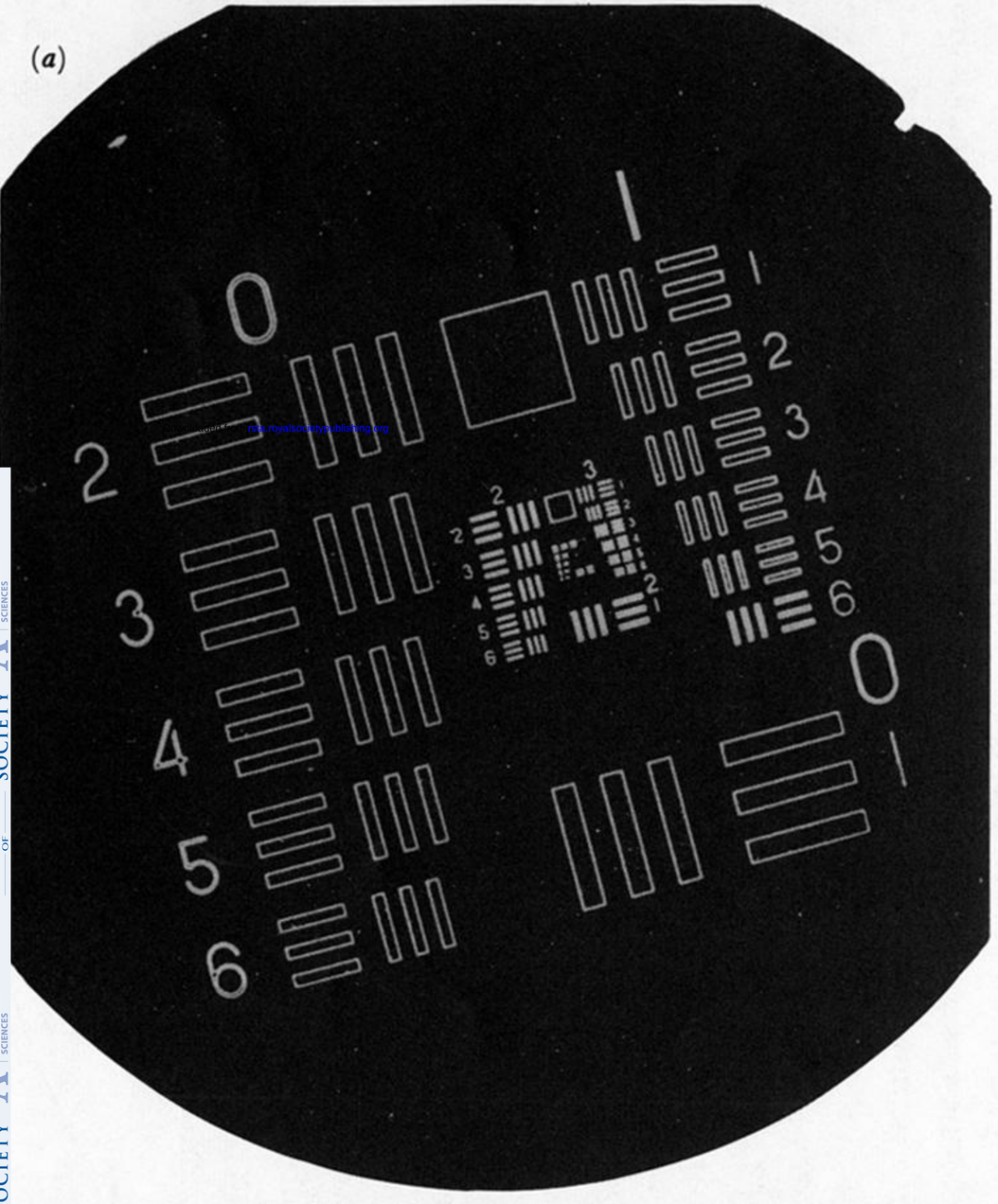

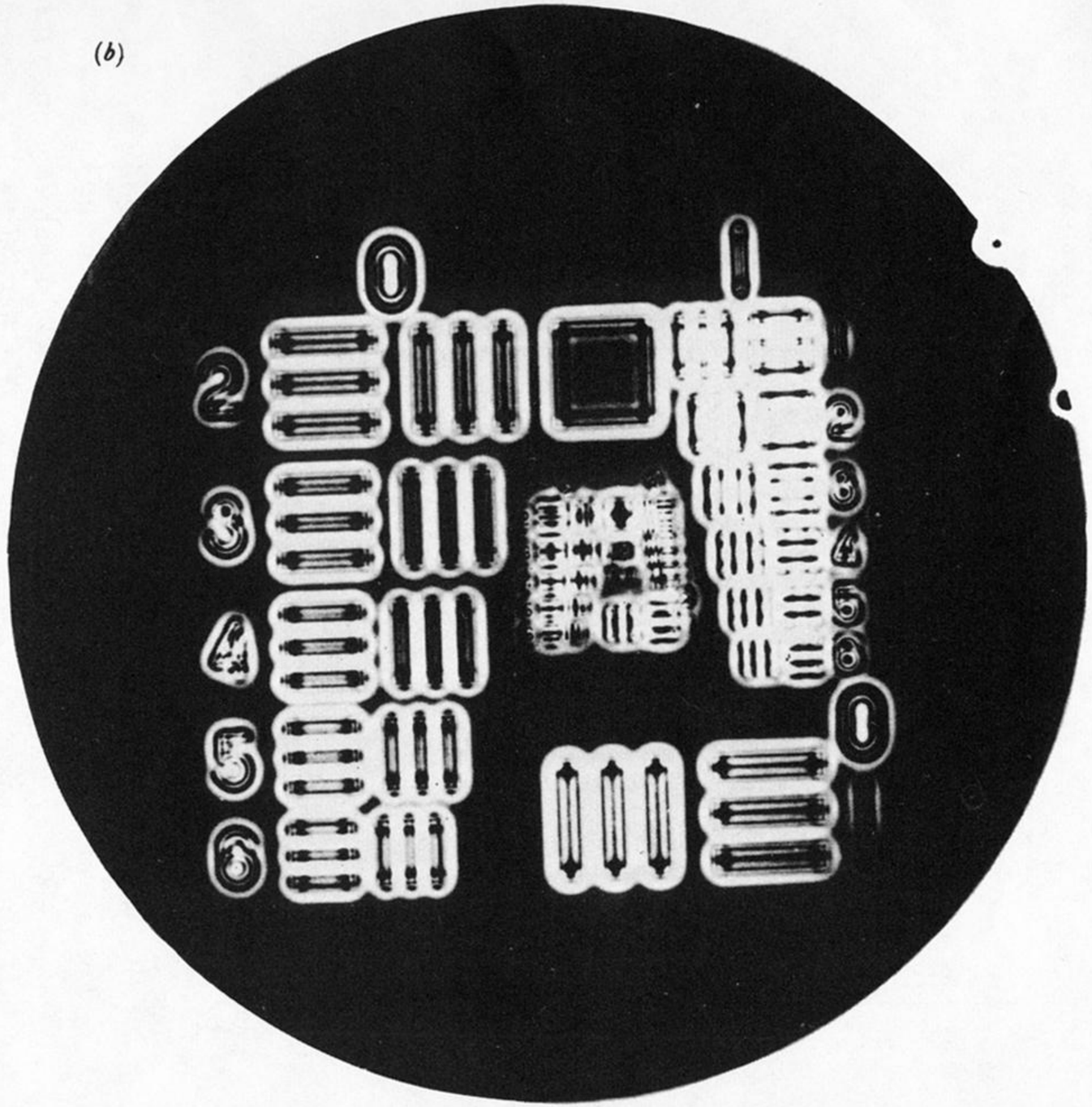

FIGURE 10. Fused quartz IC resolution plate having an overall circular diameter of 25.4 mm. Patterns are etched into glass surface with erosion lithography, $C_R = 3.48$ mm/μs, $d_{sc} = 0.04$ mm. Patterns are five sets (0, 1, 2, 3, 4) of bar-space combinations of equal width, each set one-half of the previous in size. The largest of set 0 is 0.8 mm; the largest of set 4 (not resolved in surface wave or direct reflection image) is 0.05 mm. (*a*) Direct reflection image with plate in transducer focal plane, (*b*) surface-wave image, $D_R = 0.86$ mm; 50 MHz transducer, 6.0 mm in diameter focused at 4.8 mm in water; −3 dB focal spot size in water is 25 μm.

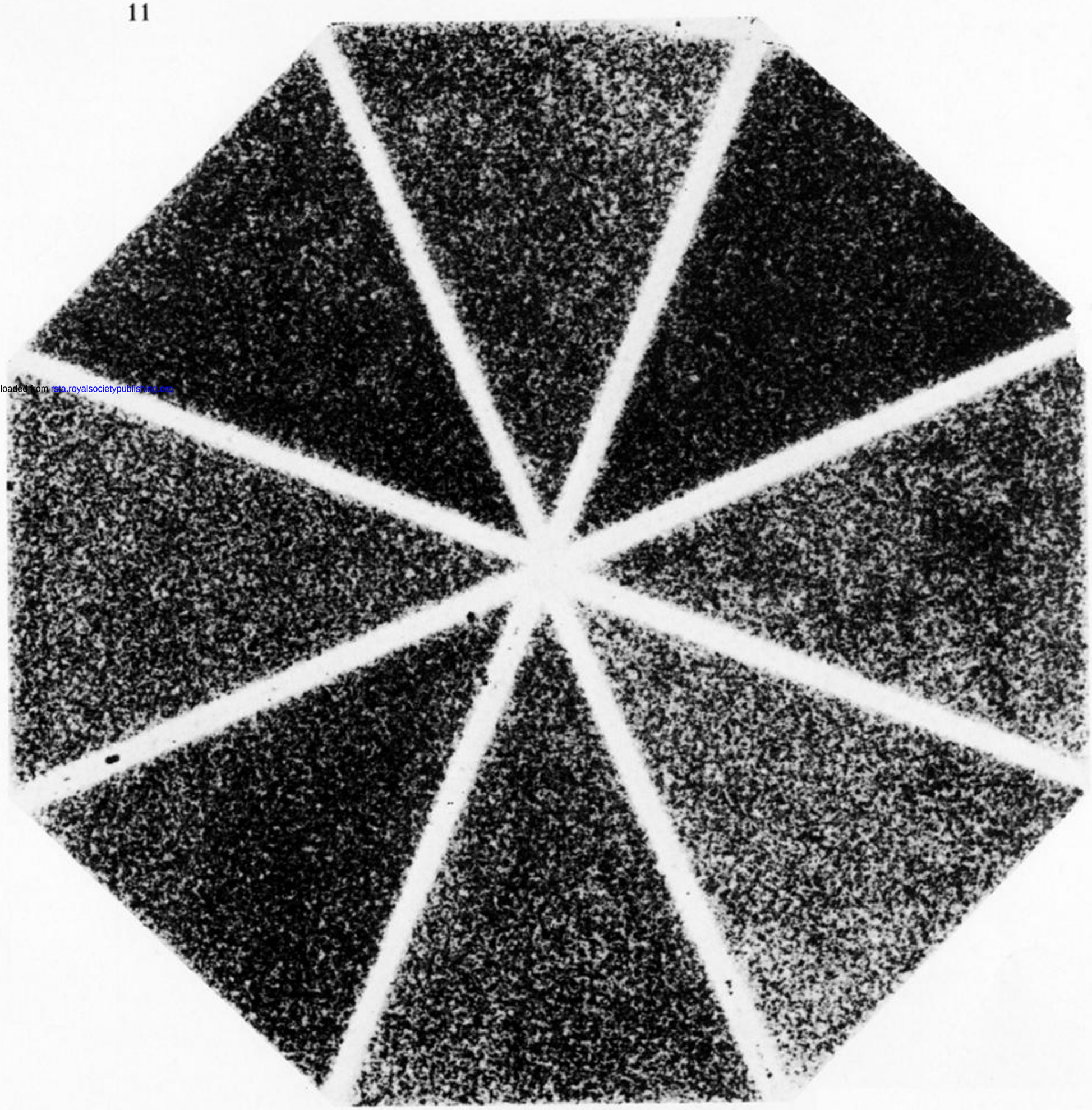

FIGURE 11. Mild steel sample composed of eight segments soldered together, $C_R = 3.04$ mm μs^{-1} in steel; 50 MHz transducer, 6.0 mm in diameter focused at 4.8 mm in water, $D_R = 0.6$ mm; sample is 35.7 mm, flat-to-flat.

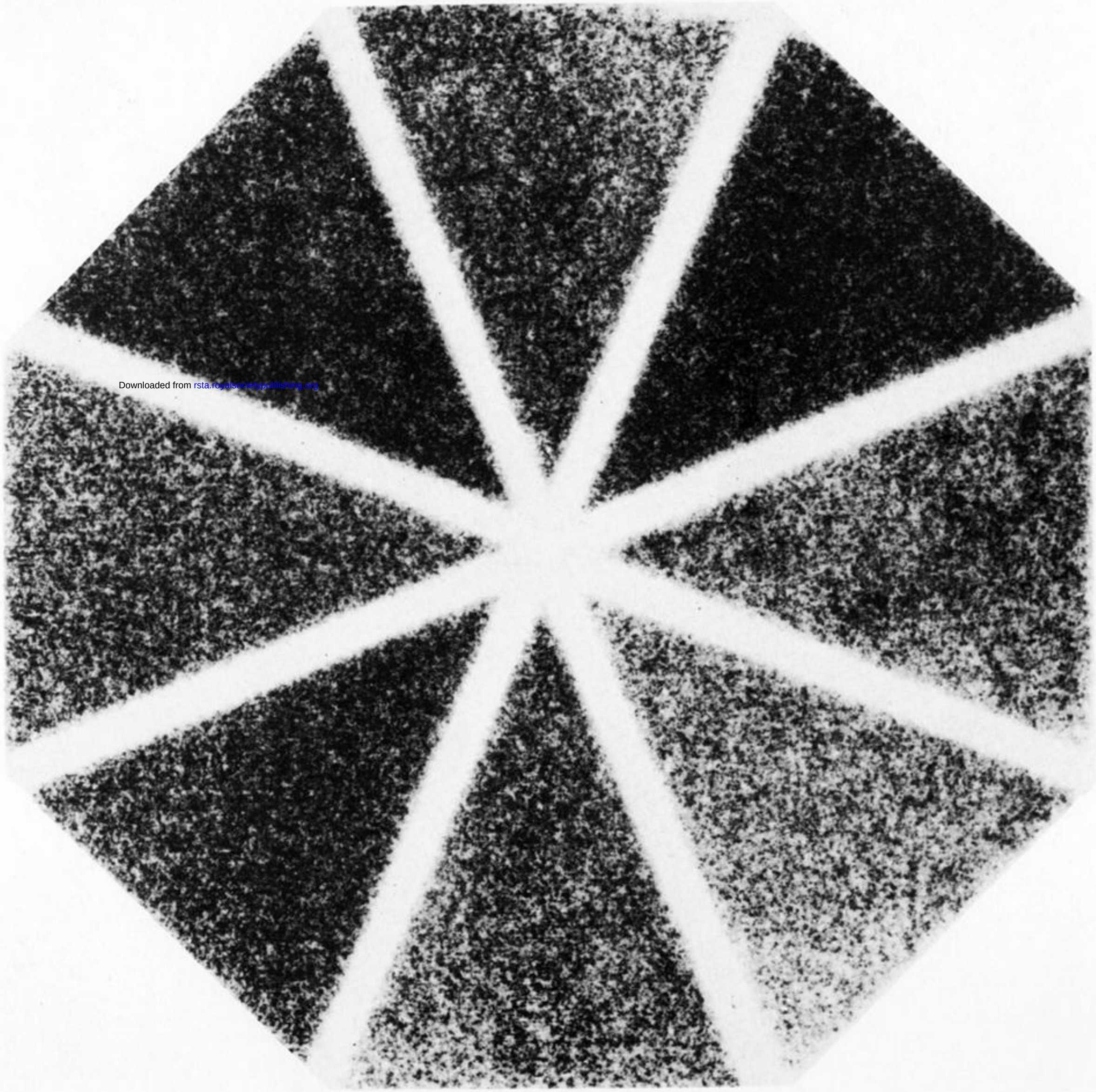

PHILOSOPHICAL TRANSACTIONS OF THE ROYAL SOCIETY A MATHEMATICAL, PHYSICAL & ENGINEERING SCIENCES

FIGURE 12. Same as figure 11, except $D_R = 1.1$ mm.

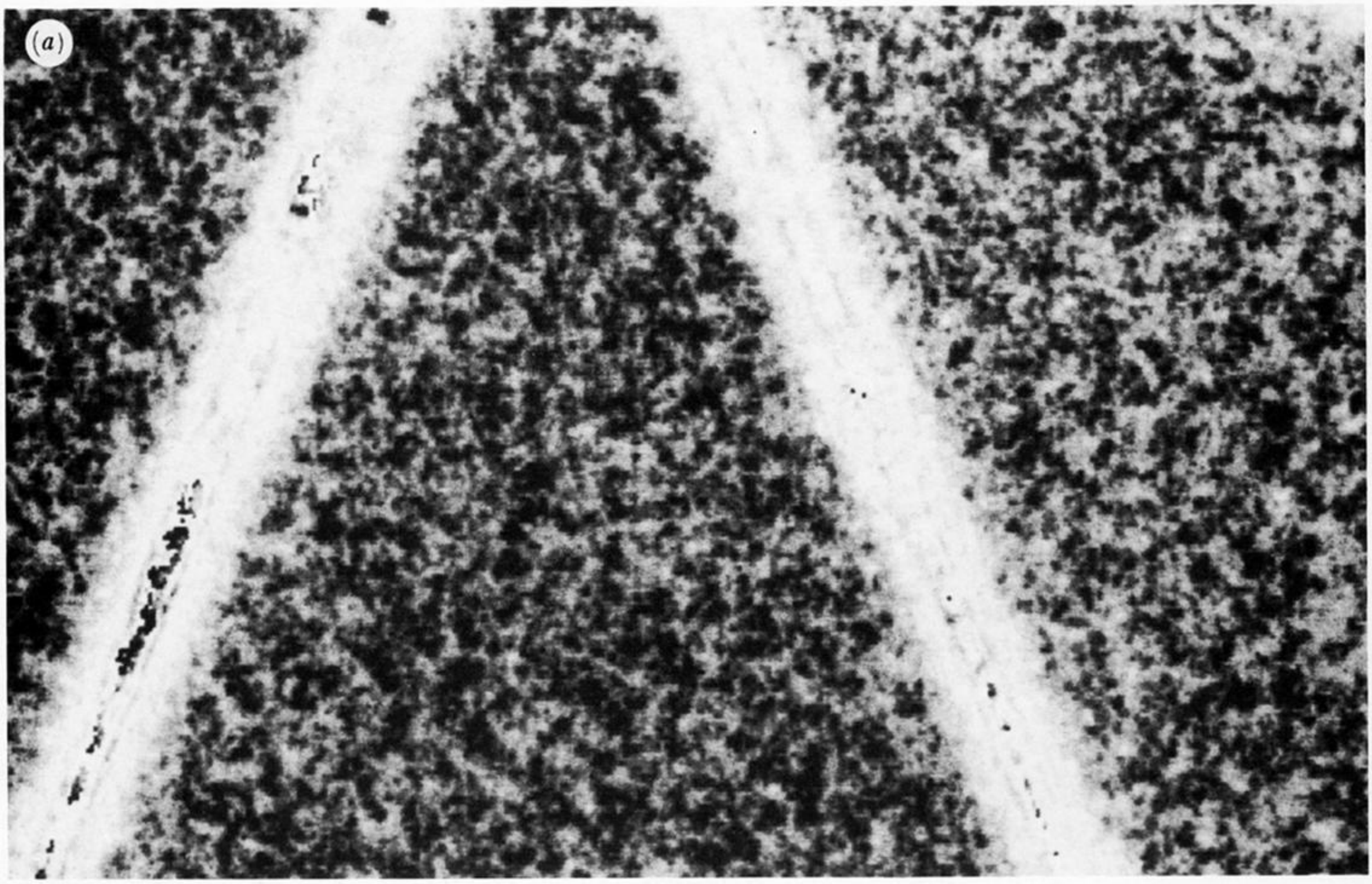

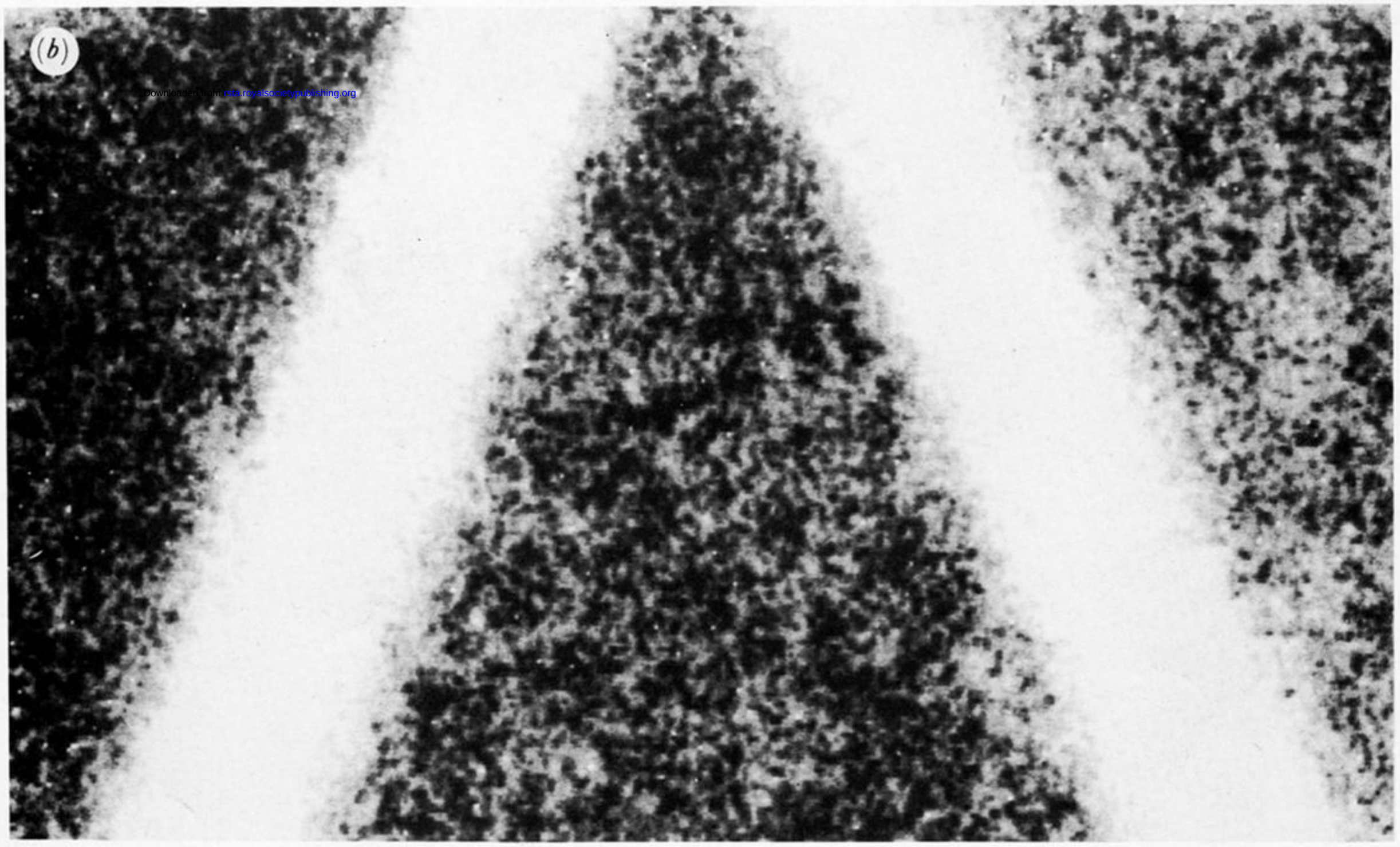

FIGURE 13. An enlarged view of the apex of the central lower segment of (*a*) figure 11 and (*b*) figure 12.

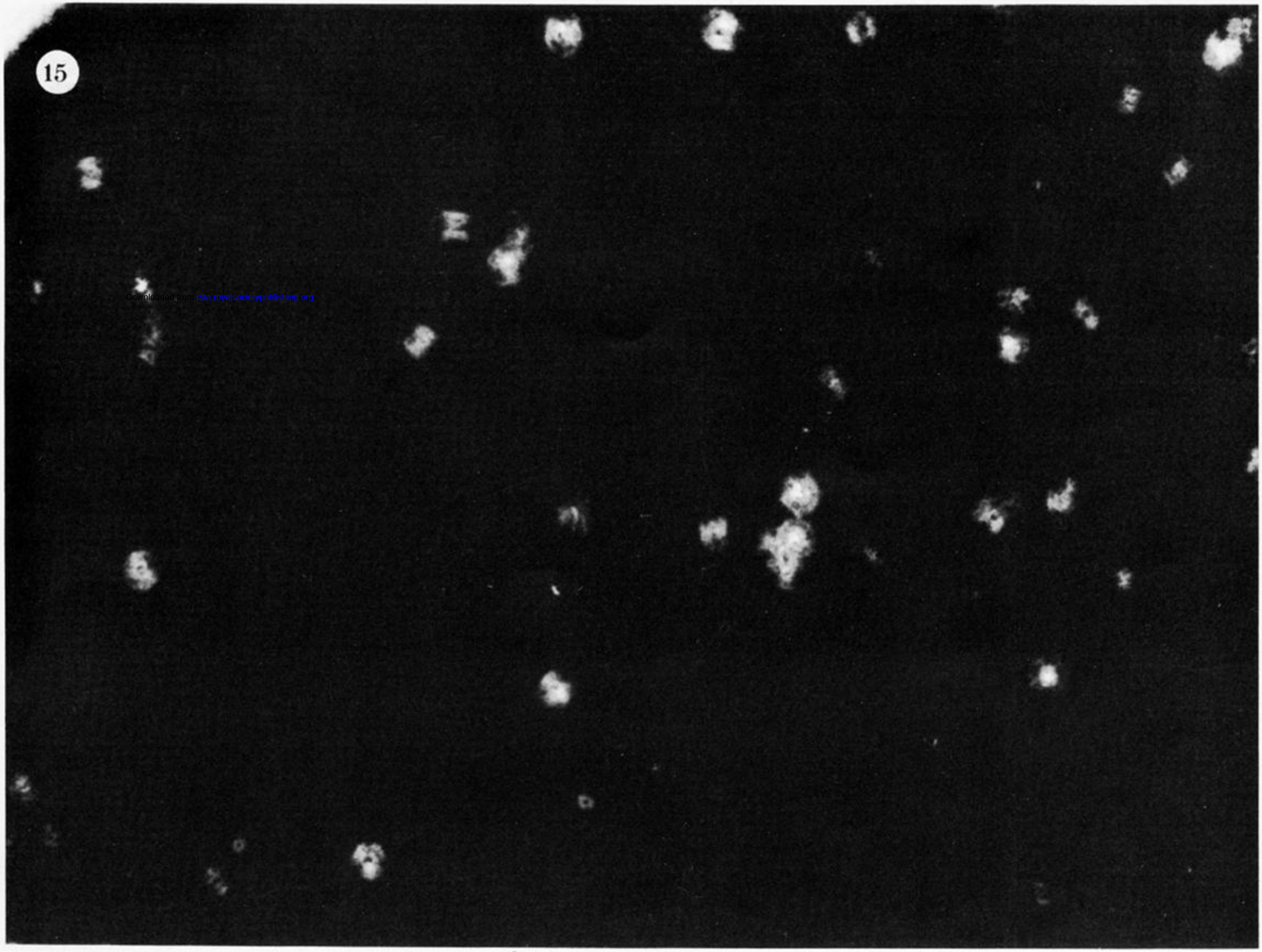

FIGURE 15. Hot isostatically pressed sample of an aircraft engine superalloy (René 95) with 0.1–0.15 mm alumina fragments sintered in the metal. Grey scale set to show only surface-breaking flaws. $C_R = 3.175$ mm μs^{-1}, $D_R = 0.46$ mm; 50 MHz transducer, 6.0 mm in diameter focused at 4.6 mm in water. Sample size is 12.5 mm × 15.62 mm.

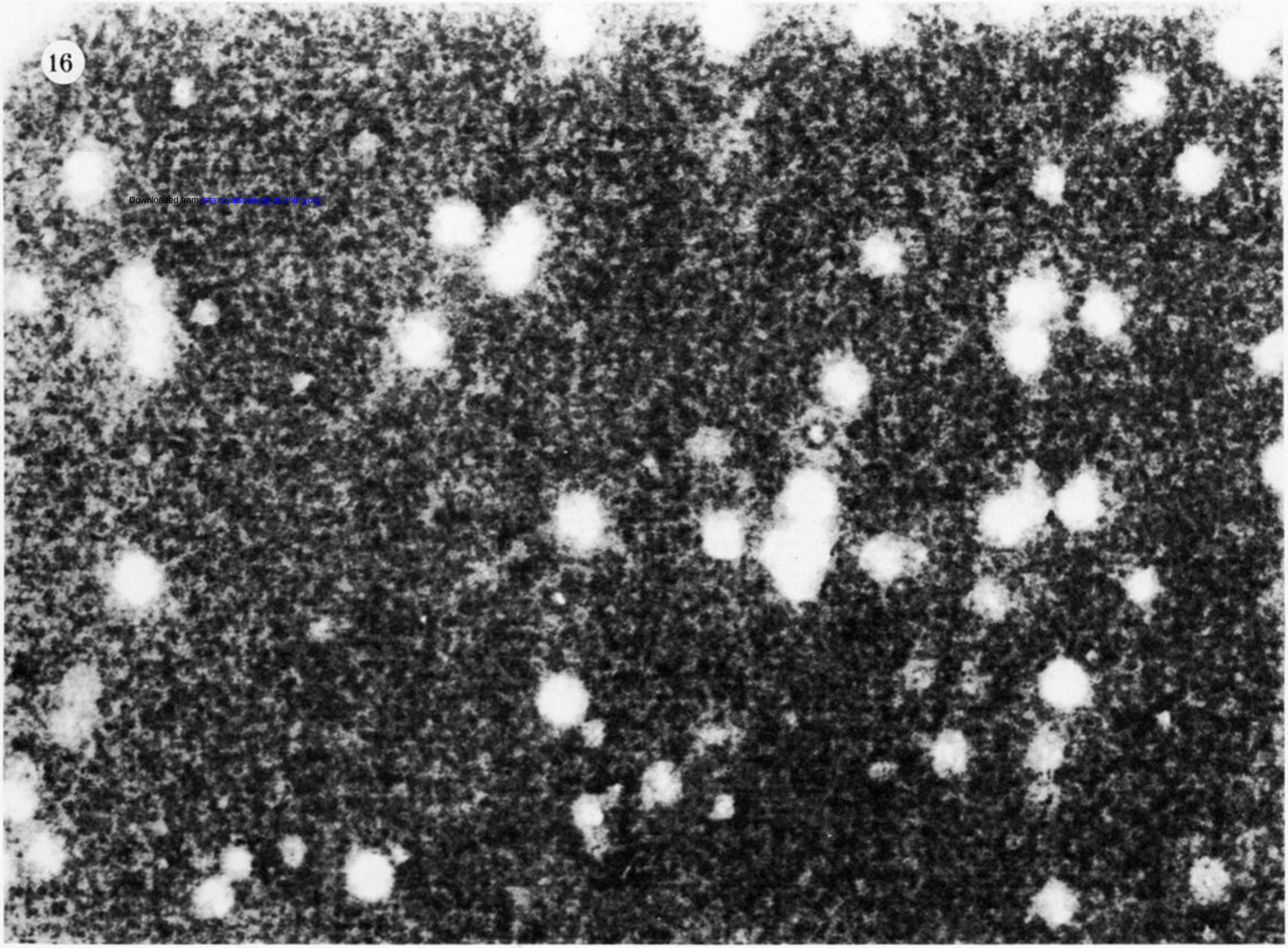

PHILOSOPHICAL TRANSACTIONS OF THE ROYAL SOCIETY A MATHEMATICAL, PHYSICAL & ENGINEERING SCIENCES

FIGURE 16. Same data file as figure 15, except grey scale now set to show detail of microstructure.

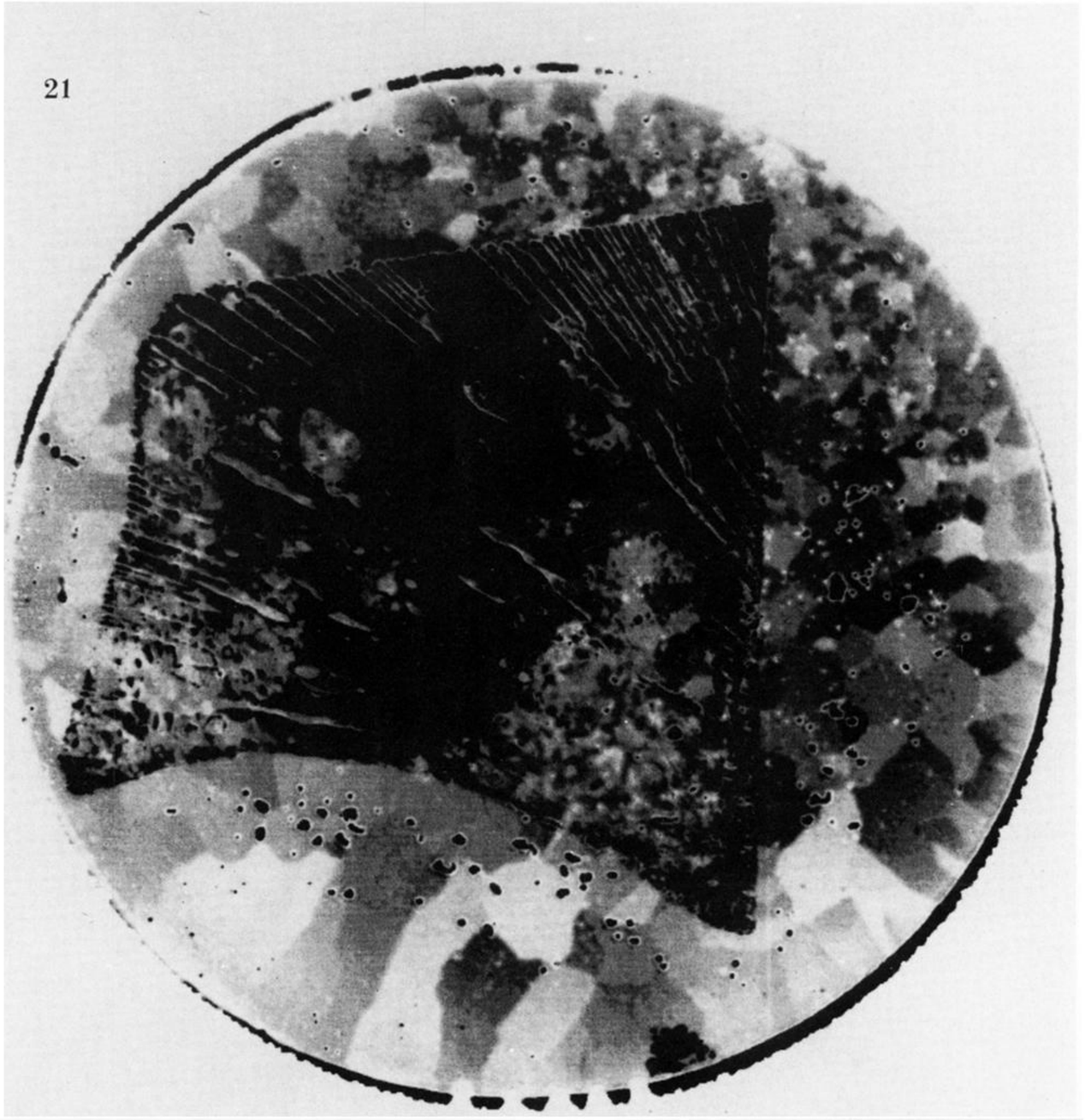

FIGURE 21. Image of solder bond-layer between two 43.0 mm silicon discs, each 0.5 mm thick. Layer was formed by melting a 0.025 mm solder foil (black outline) in a vacuum. Grey scale for figure 21 is a linear ramp adjusted to emphasize the grain size distribution in the intact portion of the solder layer. Voids and grains are readily apparent.

PHILOSOPHICAL TRANSACTIONS OF THE ROYAL SOCIETY A MATHEMATICAL, PHYSICAL & ENGINEERING SCIENCES

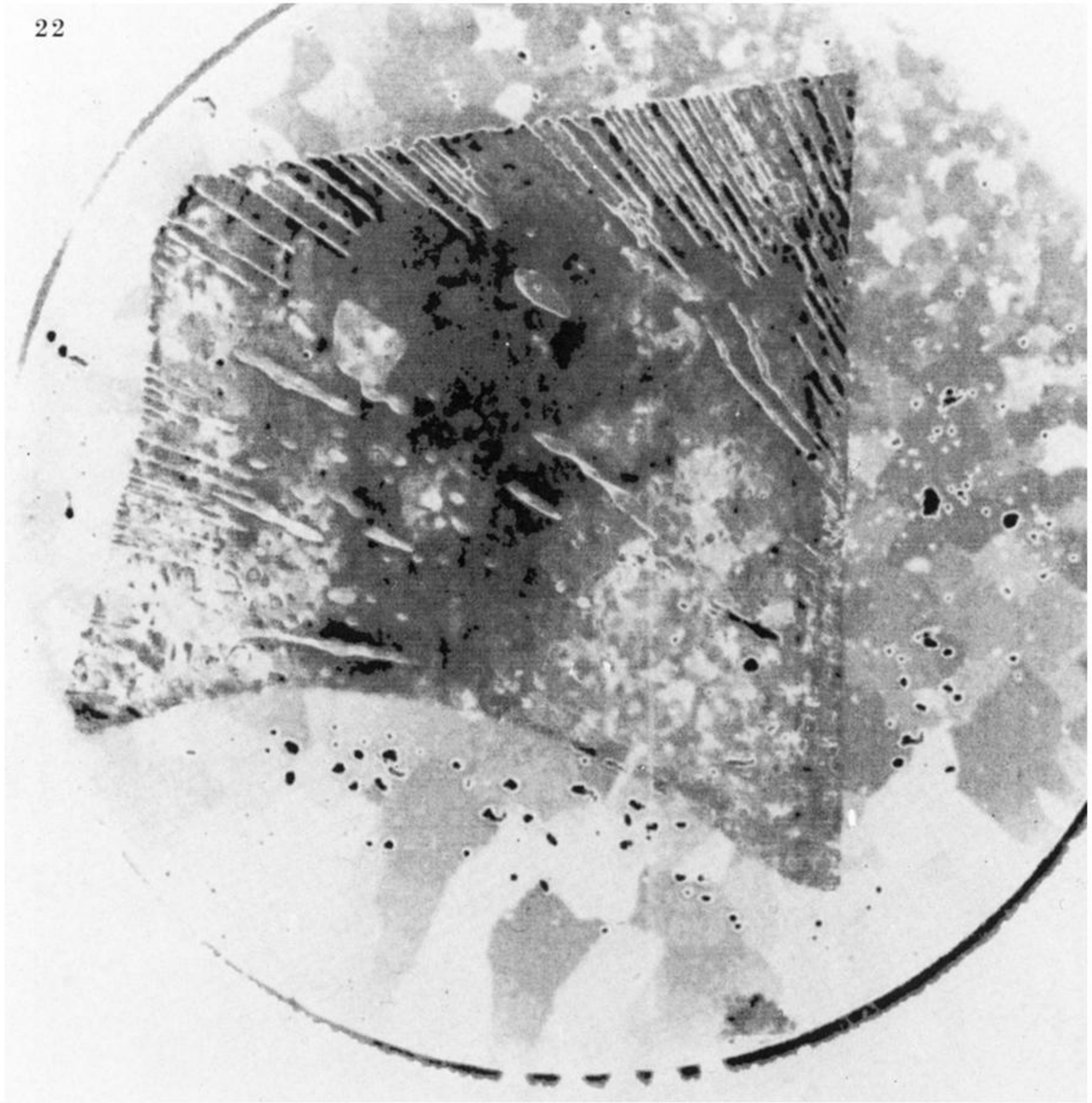

FIGURE 22. Image from same data set as figure 21. Grey scale is set by an equalized histogram algorithm, which, in this case, permits the voids and other signals of equal amplitude to be separated clearly from the remaining structure.

PHILOSOPHICAL TRANSACTIONS OF THE ROYAL SOCIETY A MATHEMATICAL, PHYSICAL & ENGINEERING SCIENCES

FIGURE 17. (*a*) Direct reflection image from obverse surface of Canadian penny; same 50 MHz transducer as figure 14, $d_{sc} = 0.025$ mm. (*b*) Reverse face of coin. The penny is 19 mm in diameter.

PHILOSOPHICAL TRANSACTIONS OF THE ROYAL SOCIETY A MATHEMATICAL, PHYSICAL & ENGINEERING SCIENCES

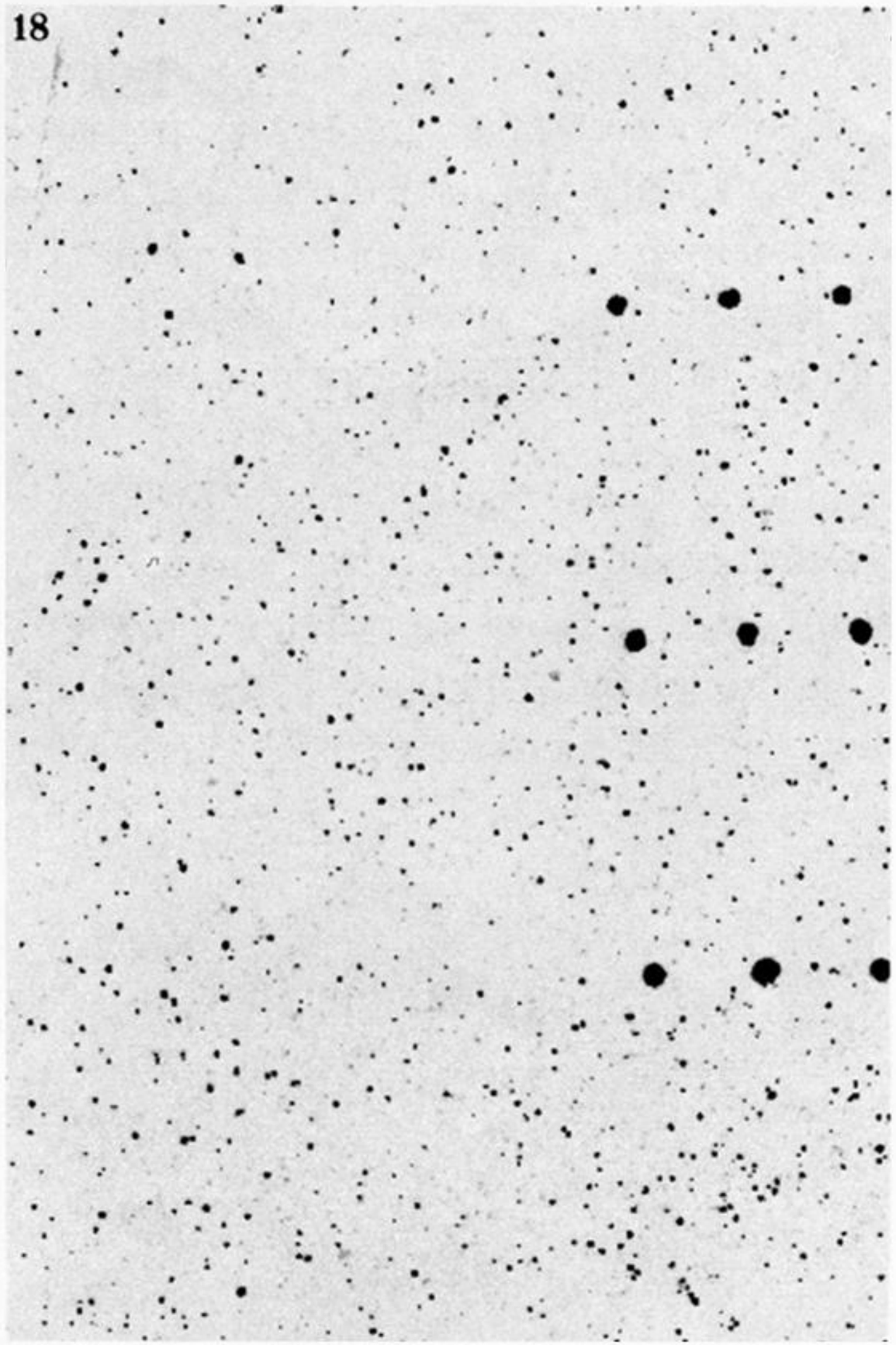

FIGURE 18. As-pressed sample of René 95 from 150 mesh powder showing 0.25, 0.375, and 0.5 mm electrodischarge machined holes and porosity, $C_L = 6.04$ mm μs^{-1}; 50 MHz transducer, 6.0 mm inn diameter focused at 12.5 mm in water, $d_{sc} = 0.06$ mm, $l_{sc'} = 0.12$ mm; plane of focus and ends of holes are both 1.5 mm deep. Sample size is 24.0 mm × 35.0 mm × 3.1 mm.

PHILOSOPHICAL TRANSACTIONS OF THE ROYAL SOCIETY A MATHEMATICAL, PHYSICAL & ENGINEERING SCIENCES

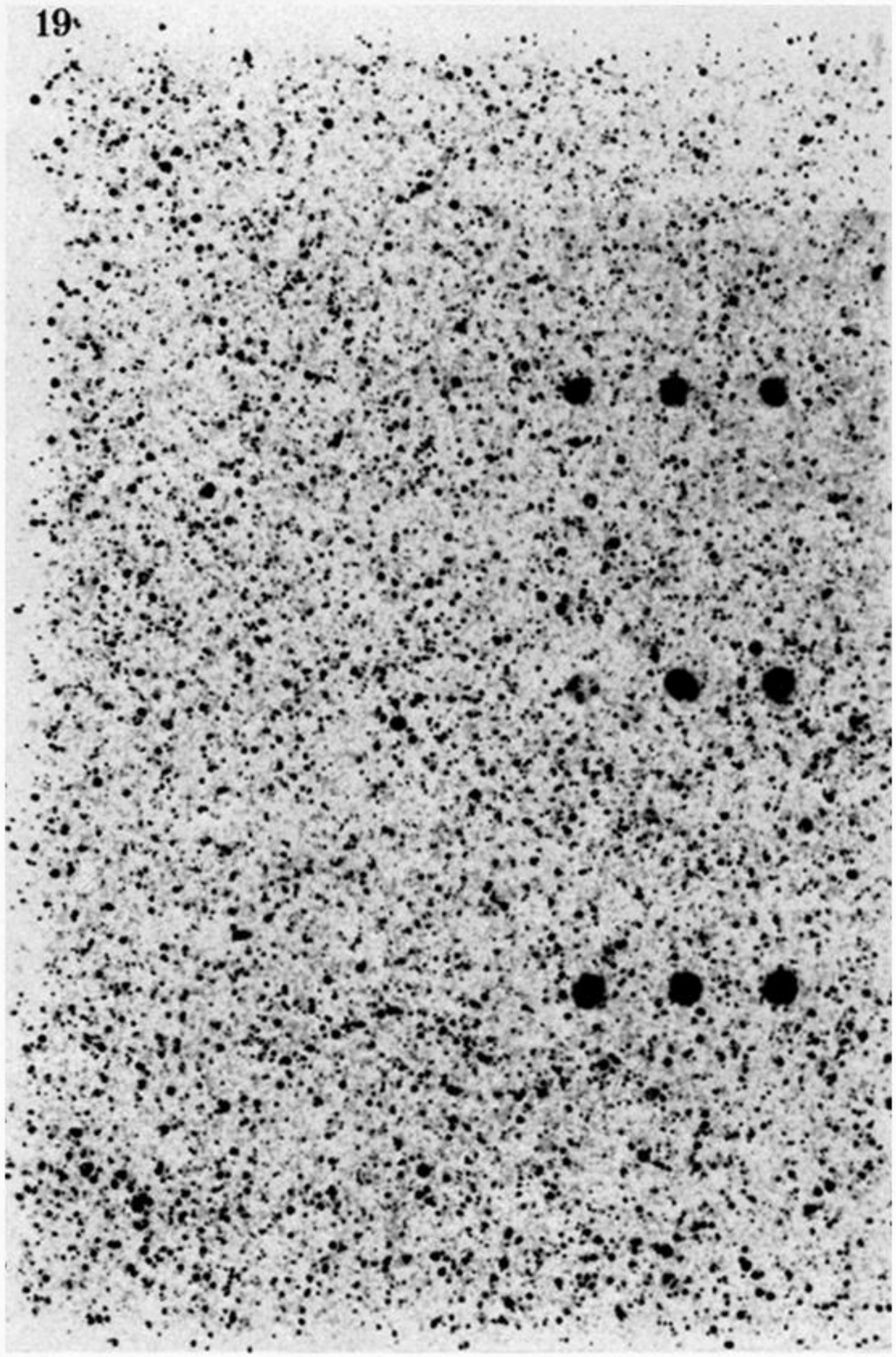

FIGURE 19. As-pressed sample of René 95 as in figure 18 but with dimensions of 24.0 mm × 35.0 mm × 6.3 mm. Plane of focus and end of holes are 3.1 mm deep; 50 MHz transducer, 6.0 mm in diameter focused to 19.0 mm in water, $d_{sc} = 0.091$ mm, $l_{sc'} = 0.27$ mm. Note the larger number of detected pores resulting from the greater depth of field.

PHILOSOPHICAL TRANSACTIONS OF THE ROYAL SOCIETY A MATHEMATICAL, PHYSICAL & ENGINEERING SCIENCES